11.4 SPATIAL VARIABILITY OF SURFACE-LEVEL METEOROLOGICAL VARIABLES OVER ARCTIC SEA ICE

Edgar L Andreas*
NorthWest Research Associates, Inc.; Lebanon, New Hampshire

1. INTRODUCTION

Global and regional climate models and weather prediction models are based on equations of motion in which the relevant variables are continuous in space and time. In the numerical representation of these models, however, space is divided into horizontal grid cells that range in size from a few kilometers to 100 km (e.g., Collins et al. 2006; Hunke et al. 2010; Bromwich et al. 2009; Tastula et al. 2012), and the assumption is that most surface-level variables have the same value over an entire grid cell. For example, the 2-meter air temperature is taken to be the same value over a climate model grid cell that may be 100 km on a side. I have data from the experiment to study the Surface Heat Budget of the Arctic Ocean (SHEBA; Uttal et al. 2002) to assess how appropriate this assumption of grid cell uniformity is over Arctic sea ice.

During the year-long SHEBA deployment (October 1997 to October 1998), the Atmospheric Surface Flux Group (ASFG; Andreas et al. 1999; Persson et al. 2002) maintained five sites with separations from one another of up to 12 km. By comparing simultaneous data between pairs of sites, I can evaluate the spatial variability of the data and, thereby, see whether various near-surface atmospheric variables lose correlation with increasing separation. For this analysis, I compare the monthly averages at each site and evaluate two spatial statistics for each season: the spatial correlation function and the bias between sites as a function of separation.

The variables that the five ASFG SHEBA sites measured include near-surface barometric pressure, wind speed, direction, air temperature, and relative humidity; surface temperature; the four broadband radiation components, incoming and outgoing longwave and shortwave radiation; and the turbulent surface fluxes of momentum and sensible heat. For each site, I also ran the bulk flux algorithm that Andreas et al. (2010a, 2010b) developed to compute the surface fluxes of momentum and sensible and latent heat. Here, I report spatial statistics for the variables pressure, air temperature, wind speed, relative humidity, surface temperature, and the measured and bulk turbulent surface fluxes.

Not only will this analysis have implications for three-dimensional modeling with climate models and weather forecast models, it is germane to one-dimensional modeling (Brun et al. 2008)—for example, with PIEKTUK-D (Chung et al. 2011), with the thermodynamic code in many sea ice models (Bitz and Lipscomb 1999; Hunke et al. 2010, 2013), and with single-column models (e.g., Lipscomb 2001; Holland 2003; Morrison et al. 2005). That is, after this analysis, we will be able to speculate on the area over which a one-dimensional model's results are valid. Likewise, this analysis will provide guidance on how far data measured on buoys drifting in sea ice can be extrapolated. Conversely, this spatial analysis can be used to decide how closely drifting buoys or other such observational platforms must be placed to provide data that cover specific regions or the entire Arctic.

Here, I divide the SHEBA data series into the four typical Arctic seasons (e.g., Lindsay 1998; Brunke et al. 2006)—autumn (September, October, November), winter (December, January, February), spring (March, April, May), and summer (June, July, August)—and calculate spatial statistics in each season.

I find that near-surface variables like pressure, air temperature, and wind speed are well correlated in all seasons up to the distance limit in our data, 12 km. Consequently, the assumption of grid cell uniformity seems appropriate for these variables—at least for grid cells of 12 km or less. Although relative humidity generally shows weaker correlation, I ultimately decide that this result is an instrumentation problem (i.e., Andreas et al. 2002; Andreas and Jordan 2013); relative humidity is thus spatially homogeneous over grid cells up to 12 km, as are the other state variables.

The measured turbulent fluxes, friction velocity (u_*) and sensible heat flux (H_s), are weakly correlated from site to site in all seasons, as turbulence variables are known to be. The bulk fluxes of u_*, H_s, and H_L, the latent heat flux, on the other hand, are better correlated because they derive from variables that are well correlated: namely, air temperature, wind speed, relative humidity, and surface temperature.

*Corresponding author address: Dr. Edgar L Andreas, NorthWest Research Associates, Inc., 25 Eagle Ridge, Lebanon, NH 03766-1900; e-mail: eandreas@nwra.com.

2. SHEBA DATA

The SHEBA Atmospheric Surface Flux Group (ASFG) dataset that I consider here comprises observations at five levels on a 20 m tower in the main SHEBA camp (Persson et al. 2002; Grachev et al. 2005). Each tower level had a three-axis sonic anemometer/thermometer from Applied Technologies, Inc. (K-type sonic), that yielded the mean wind speed and direction and the turbulent fluxes of momentum and sensible heat by eddy covariance. Each level also had instruments from Vaisala that measured mean air temperature and relative humidity.

The lower four levels on the tower were, nominally, at 2.2, 3.2, 5.1, and 8.9 m; the upper level changed from 13.8 m in winter to 18.2 m in summer (Persson et al. 2002; Brunke et al. 2006). For the temperature, humidity, and wind speed measurements analyzed here, I used data from the lowest level that reported good data. This was generally the 2.2 m level. For the measured and modeled (described later) momentum and sensible heat fluxes, I used the median values from all levels that reported good data (Andreas et al. 2010a, 2010b) because the fluxes are generally assumed to be constant over this height range.

Near this main tower were paired up-looking and down-looking Eppley broadband shortwave and longwave radiometers. These were equipped with blowers to mitigate frost formation on the radiometer domes. We calculated surface temperature with the data from the up-looking and down-looking longwave radiometers (Andreas et al. 2010a, 2010b).

Besides this main site, the Atmospheric Surface Flux Group maintained four remote sites that were 0.25 to 12 km from the tower and were off the power grid for the main SHEBA ice camp. These sites were instrumented with Flux-PAM stations (PAM means portable automated mesonet) from the instrument pool at the National Center for Atmospheric Research (Militzer et al. 1995; Horst et al. 1997). Along with the main tower, three PAM sites ran for the entire SHEBA year: Atlanta, Baltimore, and Florida.

Site Cleveland was also deployed early in the experiment but was damaged by a ridging event in early February 1998 and went off line for several months for repairs. This equipment was redeployed in early April 1998 at a site called Seattle and repositioned again in early June to a site called Maui. I will refer to the data stream from this PAM station as C-S-M (i.e., Cleveland-Seattle-Maui).

The PAM sites measured the same variables that the main ASFG site did but at one level only (cf. Brunke et al. 2006; Andreas et al. 2010a, 2010b). That is, this equipment measured wind speed, direction, air temperature, relative humidity, momentum flux, and sensible heat flux at single levels that were 2–3 m above the surface. I will henceforth refer to all of these low-level wind speed, temperature, and humidity data from both the tower and the PAM sites as the 2 m values.

The PAM stations used Vaisala sensors to measure air temperature and humidity (Andreas et al. 2002). All data from the main tower site and these PAM sites were averaged hourly. In my subsequent analyses, I use these hourly data in all calculations.

Each PAM site measured broadband incoming and outgoing longwave ($Q_{L\downarrow}$ and $Q_{L\uparrow}$, respectively) and shortwave radiation ($Q_{S\downarrow}$ and $Q_{S\uparrow}$) with Eppley and Kipp and Zonen radiometers, respectively. Because of high relative humidity throughout the year (Andreas et al. 2002), the domes of these radiometers were prone to frost formation that compromised their measurements. And such icing was not obvious in the individual radiometer data. In March and early April 1998, however, all PAM radiometers were fitted with heaters and blowers that kept the domes virtually ice free through the end of the experiment.

I will not talk specifically about the radiative fluxes because we describe them elsewhere (Andreas and Jordan 2013, 2015). I mention them, however, because I calculated the surface temperature, Θ_s, from the measured longwave radiative fluxes according to (e.g., Andreas et al. 2010a, 2010b)

$$\Theta_s = (\sigma \varepsilon)^{-1/4} \left[Q_{L\uparrow} - (1-\varepsilon) Q_{L\downarrow} \right]^{1/4} . \tag{1}$$

In this, ε (= 0.99) is the surface emissivity and σ (= 5.67051×10^{-8} W m^{-2} K^{-4}) is the Stefan-Boltzmann constant. Because $Q_{L\uparrow}$ and $Q_{L\downarrow}$ are hourly averages, Θ_s is the hourly value. I later use Θ_s in the bulk flux algorithm.

For measuring wind speed, direction, and the turbulent momentum and sensible heat fluxes, each PAM site was originally deployed with a Gill R2 Solent sonic anemometer/thermometer. The icing also affected these sonics. We noticed, however, that the Applied Technologies sonics on the main tower shed this frost better than these Gill sonics. Hence, by the end of February 1998, we had replaced the Gill sonics on all the PAM sites except Florida (which was near the main camp and easiest to maintain) with sonics from Applied Technologies.

As a second measure to prevent frost formation, we installed heaters on all the PAM sonics by the end of February 1998. Unlike the radiometers, the sonics could identify bad data. This data quality indicator was the percentage of good 10 Hz samples collected during

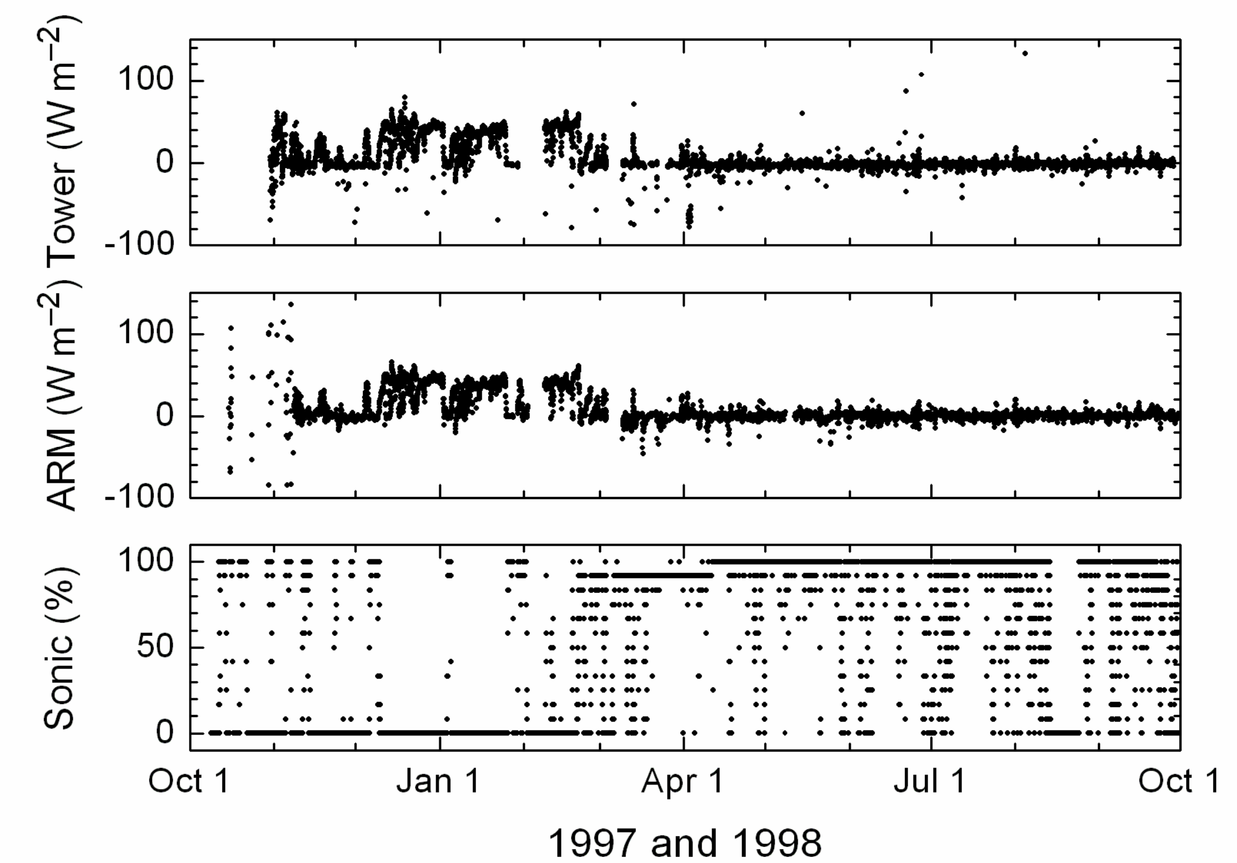

FIG. 1. Examples from PAM site Atlanta of the hourly radiometer and sonic metrics for the duration of SHEBA. The "Tower" radiometer metric is the difference between the incoming longwave radiation measured at Atlanta and near the main ASFG tower. The "ARM" metric compares the Atlanta incoming longwave radiation with the simultaneous measurement at the SHEBA Atmospheric Radiation Measurement site. The "Sonic" metric is the percentage of good data from the Atlanta sonic anemometer/thermometer during an hour.

an hour (Fig. 1). When that percentage fell below 99.5%, the heaters turned on automatically and ran until the percentage of good data was again above 99.5%. In using data from the PAM sonics, I retained for analysis only hours with at least 20% good data (i.e., 12 good minutes during an hour; Table 1).

I also screened for icing when evaluating the quality of the PAM radiometer data to retain for analysis. The PAM data files contain two metrics for evaluating icing (www.eol.ucar.edu/isf/projects/sheba/rad.isff.html) that I will henceforth refer to as *radiometer metrics*. Beside the ASFG radiometers near the main tower, which were well maintained and had efficient blowers, the Atmospheric Radiation Measurement (ARM) program also maintained a suite of radiometers in the main SHEBA camp. The two PAM radiometer metrics compare simultaneous measurements of incoming longwave radiation at each PAM site with the incoming longwave radiation measured at the *Tower* and *ARM* sites (i.e., PAM – Tower and PAM – ARM; Fig. 1). When frost was present on the dome of an up-looking PAM longwave radiometer, that radiometer essentially sensed the near-surface air temperature, not the sky temperature. As a result, a frosted PAM radiometer would generally yield higher values of incoming longwave radiation than would the clean tower or ARM up-looking radiometer.

Figure 1 shows hourly time series of these two radiometer metrics for PAM site Atlanta. During the first four months of the experiment, before the PAM radiometers had effective blowers and heaters, both the tower and ARM radiometer metrics were often large positive numbers. This is the signal of frosted PAM radiometers. During this same period, the Atlanta sonic corroborates this diagnosis of icing events by showing corresponding periods of few good sonic samples (Fig.

TABLE 1. Screening for quality of the variables from each PAM site. As discussed in the text, variables from the main tower site were largely unaffected by frost formation but were screened for data quality using objective and subjective criteria before being compiled for the current analysis (Persson et al. 2002; Grachev et al. 2007). For brevity, the manuscript does not discuss all of the variables in this table, but all are available in all five datasets.

Variable	Screening
Pressure	PA*
Air Temperature	PA
Relative Humidity	PA
Wind Speed	SC**
Wind Direction	SC
Incoming Longwave Radiation	RM***
Emitted Longwave Radiation	RM
Incoming Shortwave Radiation	RM
Reflected Shortwave Radiation	RM
Surface Temperature	RM
Measured Friction Velocity	SC
Measured Sensible Heat Flux	SC
Bulk Friction Velocity	SC, RM
Bulk Sensible Heat Flux	SC, RM
Bulk Latent Heat Flux	SC, RM

*PA indicates that the only test is whether the variable is present or absent in the dataset for a given hour.
**In addition to the present or absent test, the variable is tested for sonic counts (SC). Only values based on at least 20% good data for an hour are considered.
***Besides the present or absent test, data are subjected to a test of the radiometer metric (RM). An hourly value is retained only if RM < 20 W m^{-2}, where RM compares the longwave radiation at a given PAM site with either the tower or ARM longwave radiation.

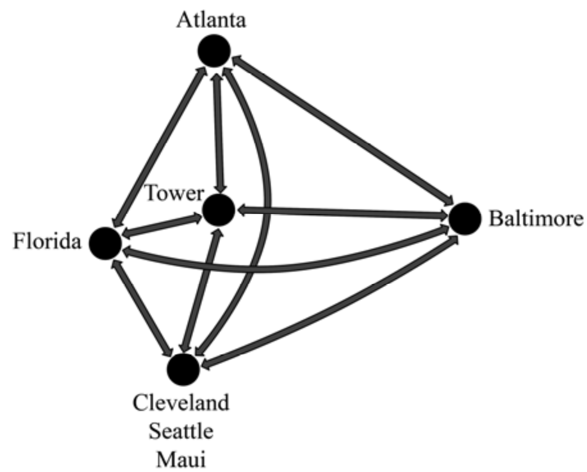

FIG. 2. At any given hour, the five SHEBA sites taken two at a time for the spatial analysis provide 10 potential separation distances.

1). In my analysis, I conservatively rejected because of presumed icing any radiative fluxes for which the PAM – Tower radiometer metric was greater than 20 W m^{-2}. If the tower radiometer metric was unavailable, I tested the PAM – ARM radiometer metric for the same limit.

Table 1 summarizes this screening for sonic and radiometer icing and notes which variables are affected by the screening. Because computations of the turbulent fluxes from the SHEBA bulk flux algorithm require both surface temperature and wind speed, the bulk friction velocity and the sensible and latent heat fluxes face double jeopardy with this screening.

Figure 2 shows the connections among the sites. For calculating spatial statistics (described shortly), I look at simultaneous values of the same variable from paired sites. Because I have five sites and am looking for pairs, I evaluate the number of combinations when five objects are considered two at a time to be ten. In other words, each hour can provide up to ten different distances to use for computing the spatial statistics for any of 15 variables.

Each of the five ASFG locations also had a GPS that reported hourly latitude (Θ) and longitude (Φ). If (Θ_A, Φ_A) represents the latitude and longitude at site A and if (Θ_B, Φ_B) represents the latitude and longitude at site B, I calculated the distance D between the two sites as (e.g., Weaver and Mirouze 2013)

$$D = R\Delta\Omega . \tag{2}$$

Here, R (= 6372.8 km) is the radius of curvature of the Earth, and

$$\Delta\Omega = 2\arcsin\left\{\left[\sin^2\left(\frac{\Delta\Theta}{2}\right) + \cos\Theta_A \cos\Theta_B \sin^2\left(\frac{\Delta\Phi}{2}\right)\right]^{1/2}\right\} \tag{3}$$

is the arc length, where $\Delta\Theta = \Theta_A - \Theta_B$ and $\Delta\Phi = \Phi_A - \Phi_B$.

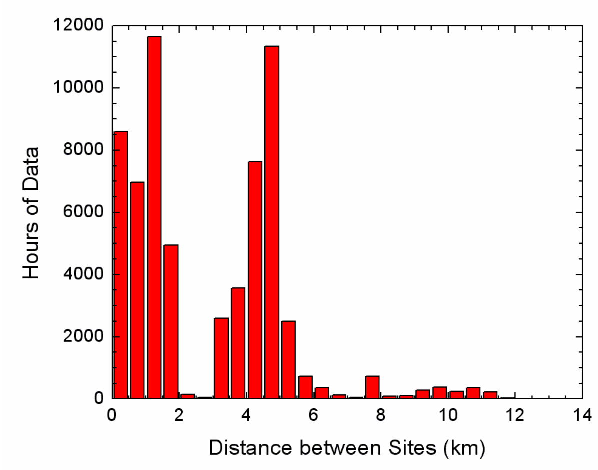

FIG. 3. This histogram shows the number of hours of unique site pairings that are available within the SHEBA dataset for each distance interval of 0.5 km.

Figure 3 shows a histogram of the hours of unique data available for each distance. Each distance bin in the figure is 0.5 km wide.

From the figure, we see that the vast majority of separations in our dataset are 6 km and less. Most of the separations beyond 6 km occurred in September 1998, when Baltimore drifted rapidly away from the other instruments. That is, the largest separations arise from September data when Baltimore is paired with the other four sites.

3. SHEBA SITES

Although several other papers have documented the snow and ice characteristics of the SHEBA sites and the overall physical features of the SHEBA area (e.g., Uttal et al. 2002; Persson et al. 2002; Sturm et al. 2002; Perovich et al. 2003), for completeness, I briefly describe the five ASFG sites.

At the beginning of the experiment, in October 1997, the snow cover was only a few centimeters deep at all sites. Snow collected episodically through the winter and typically reached a maximum average depth of about 0.4–0.5 m near May 15, 1998. The snow depth, of course, varied quite a bit horizontally about this average depending on the topography of the underlying sea ice (e.g., Sturm et al. 2002).

The snow began melting rapidly in early June and disappeared between June 14 and July 4, 1998, depending on the site, to expose bare sea ice. The ice surface continued melting at all sites into early August. Snow began falling and accumulating around September 1, and all sites had a few centimeters of snow when we discontinued measurements in late September 1998.

The sea ice experienced a similar annual cycle. At all sites, the ice grew on its underside through the winter. At roughly the time when the snow cover disappeared at a site, the ice began melting there from below. The ice generally melted at its surface and on its bottom faster than it formed during the winter such that, through the SHEBA year, the sea ice in the vicinity of the SHEBA camp thinned.

All sites were on ponded ice during the summer, nominally from June 10 until August 10, 1998. The areal coverage of melt ponds in the vicinity of the SHEBA camp reached a maximum of 22% around August 1, 1998 (Perovich et al. 2002; Andreas et al. 2010a).

The ASFG tower site and the PAM site at Florida, which was nearby, were placed on a smooth, multiyear floe that was 2 m thick at the time of deployment. Florida began reporting on October 22, 1997; on October 31, 1997, the tower site was the last ASFG equipment to come online. This ice flow thickened to 2.5–2.8 m through the winter and thinned to about 1.5 m by the end of the deployment.

On October 11, 1997, PAM site Atlanta was also deployed on a smooth, multiyear flow. This flow, however, was only 1.5 m thick at the time. Through the winter, the ice grew to over 2 m thick by early July 1998. It then thinned rapidly from top and bottom melting such that the ice was less than a meter thick when we dismantled Atlanta on September 30, 1998.

On October 12, 1997, we deployed the Baltimore PAM site on first-year sea ice in a refrozen polynya. This polynya was about 400 m north-south by 150 m east-west; the PAM site was near the southern edge. Multiyear, hummocky ice, some of which was over 3 m thick, surrounded the polynya. Ice in the polynya itself was 0.4 m thick at the time of deployment, thickened to about 1.4 m by mid-May 1998, then thinned to about 1 m by the time we decommissioned Baltimore on September 21.

We deployed site Cleveland on October 15, 1997, in a rubble field that extended a few hundred meters in all directions. I know of no measurements of the ice thickness here but presume that the sea ice was at least 3 m thick. A ridging event in early February damaged the equipment at this PAM site, and it was taken out of service on February 6.

After repairs, the station was redeployed at site Seattle on April 16, 1998. The station itself was placed on a refrozen melt pond of 50–60 m radius, but the surrounding ice beginning 100–200 m from the station in all directions was hummocky. In early June, this site became untenable because of ice motion, and the equipment was moved to new site Maui on June 10.

During the two month record from Seattle, the ice at the PAM site was 1–1.5 m thick.

Maui was on a multiyear floe with gently rolling hummocks. There are no known thickness measurements from the site, but I presume that the sea ice was at least 2 m thick at the time of deployment. Maui was an active site with frequent leads and melt ponds near it until freeze-up started around September 1. We decommissioned Maui on September 20, 1998, when ice motion upset the PAM tripod and jeopardized the equipment.

4. QUANTIFYING THE SPATIAL VARIABILITY

4.1. Monthly Averages

As context for later calculations, I computed the monthly averages of surface-level pressure, 2 m air temperature, 2 m wind speed, and surface temperature, Figs. 4–7, respectively. In each figure, the monthly average is plotted at the middle of the month. For these and all subsequent plots, I invoked the screening for frost summarized in Table 1.

In each of Figs. 4–7, the averages from April 1998 through the end of the experiment in September are very close. This is the first clue that the spatial variability over the SHEBA site from late spring through early autumn was not severe. In each figure, the error bars are ± 2 standard deviations in the monthly average. Therefore, if error bars from different sites overlap, we have 99.8% confidence that the two monthly means are statistically the same. Alternatively, if error bars do not overlap, we can reject at the 0.2% significance level the hypothesis that the monthly averages at the two sites were the same.

Extenuating circumstances, however, explain most of the obvious discrepancies among sites during the first six months of the experiment. Before computing the averages in Figs. 4–7, I screened the data from the PAM sites for cases of sensor icing (see Table 1) and ignored hours for which the quality metrics suggested icing. Figure 8 shows the number of hours of good data for each month from each site that went into computing the averages depicted in Figs. 4–7.

As Table 1 shows, I did three types of screening. The barometric pressure, air temperature, and relative humidity sensors were unaffected by icing. The “Pressure” panel in Fig. 8 shows data returns from the pressure sensors and thus represents this class of icing-resistant instruments. Likewise, the “Sonic” panel shows data returns for wind speed and is therefore also relevant to wind direction and to both the measured and bulk turbulent fluxes. Finally, the “Radiometer” panel shows returns from the up-looking longwave radiometers. This panel is relevant to every variable that relies on a radiation measurement: both incoming and outgoing longwave and shortwave radiation, surface temperature, and the fluxes calculated from the bulk flux algorithm (which requires surface temperature in the iteration).

Data returns from the PAM sonic anemometers became much more reliable in March 1998, when we began installing heaters on all the sonics. Likewise, the PAM radiometers got more reliable in March when we fitted the radiometers with heaters and blowers. The tower instruments were the last ones to come online; that is the reason for the small number of observations from the tower in October 1997. Similarly, in September 1998, Baltimore and Maui were decommissioned around September 20 while the other sites remained in operation longer.

By comparing the counts of good data in Fig. 8 with the averages in Figs. 4–7, we can explain some of the obvious discrepancies among the monthly averages. For example, the outlying pressure in October 1997 from the tower (Fig. 4) resulted because the tower sensor, which came online late, did not sample some of the higher pressures from earlier in October. Similarly, the C-S-M PAM station was mostly out of service in March 1998; its March pressure (Fig. 4) thus does not come from the same range of air masses as for the other four sites.

Comparing averages of the 2 m wind speed (Fig. 6) with the monthly retrieval rates (Fig. 8) reveals features of the instrument icing. When the tower sonics were fully operational, starting in November 1997, until March 1998, when the PAM sonics all got heating, the monthly averaged wind speed from the tower is markedly lower than for the PAM sites. Figure 8 shows that there were many more hours of good data from the tower sonics than from the PAM sonics during this period. From Fig. 6, it is therefore obvious that the tower wind speeds represent typical fall and winter conditions. Meanwhile, the PAM sonics provided good data only when the winds were high enough to preclude icing conditions or to blow any collected frost off the sonics.

4.2. Spatial Correlation Function

To compute the spatial correlation function for variable V in each season, I start by computing the covariance (Cov) for variable V between sites A and B (see Fig. 2) when they have separation D, where D represents the averaging interval $[D_{-}, D_{+})$ and $D_{+} - D_{-} = 0.5\,\mathrm{km}$. That is, I compute this covariance as

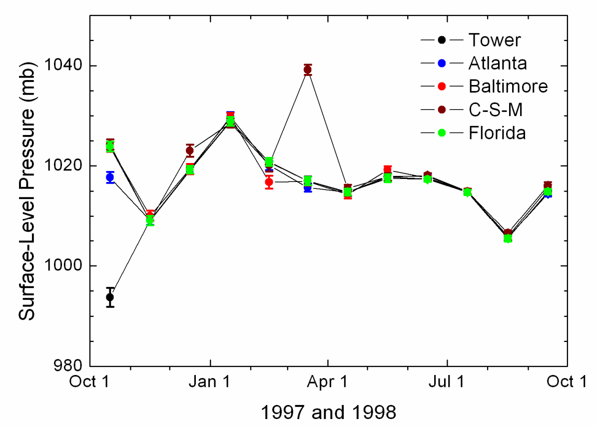

FIG. 4. Monthly averages of surface-level pressure from the five sites maintained by the SHEBA Atmospheric Surface Flux Group. The error bars are ±2 standard deviations in the monthly mean.

$$\mathrm{Cov}_{V,AB}(D) = \frac{1}{N_D}\sum_{i=1}^{N_D}\left[V_{Ai}(P_A) - \overline{V}_{AD}\right]\left[V_{Bi}(P_B) - \overline{V}_{BD}\right]. \quad (4)$$

Here, P_A, for example, is the position of site A, represented as (Θ_A, Φ_A), and N_D is the number of good A and B pairs for variable V that are in distance interval $[D_-, D_+)$ for a given season. Subscript i is the index for a specific hour in the dataset. Furthermore,

$$\overline{V}_{XD} = \frac{1}{N_D}\sum_{i=1}^{N_D} V_{Xi}(D) \quad (5)$$

is the average of these same data, where X denotes either site A or B.

To calculate the spatial correlation function, I also need the standard deviations (σ_V) for sites A and B for

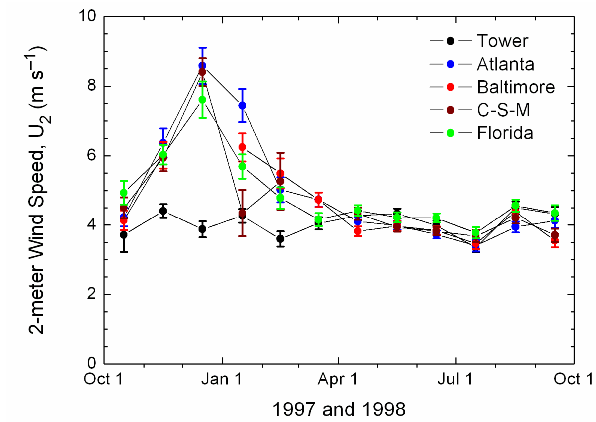

FIG. 6. As in Fig. 4 but surface-level (nominally at 2 m) wind speed (U_2).

variable V for the given season when the separation is in the distance interval $[D_-, D_+)$. These come from the variances as

$$\sigma^2_{V,X}(D) = \frac{1}{N_D}\sum_{i=1}^{N_D}\left(V_{Xi} - \overline{V}_{XD}\right)^2, \quad (6)$$

where subscript X again denotes either site A or B.

From (4), (5), and (6), I ultimately compute the spatial correlation function for variable V, separation D, a given season, and sites A and B as

$$\rho_{V,AB}(D) = \frac{\mathrm{Cov}_{V,AB}(D)}{\sigma_{V,A}(D)\sigma_{V,B}(D)}. \quad (7)$$

This $\rho_{V,AB}$ has the same properties as usual correlation coefficients. It ranges from –1.00 to +1.00. If $N_D = 1$, it is undefined because both variances are zero. If $N_D = 2$, $\rho_{V,AB}$ is exactly +1.00 or –1.00: Two

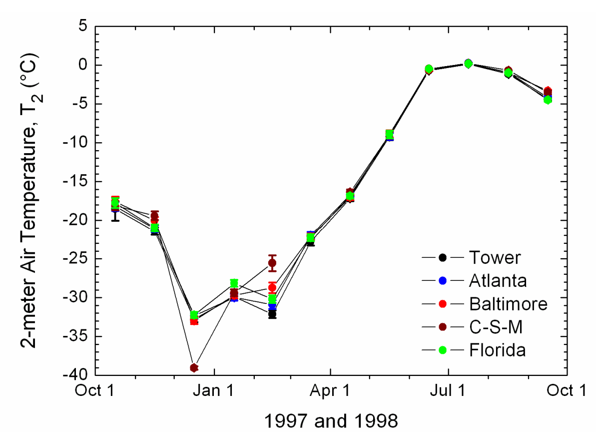

FIG. 5. As in Fig. 4 but surface-level (nominally at 2 m) air temperature (T_2).

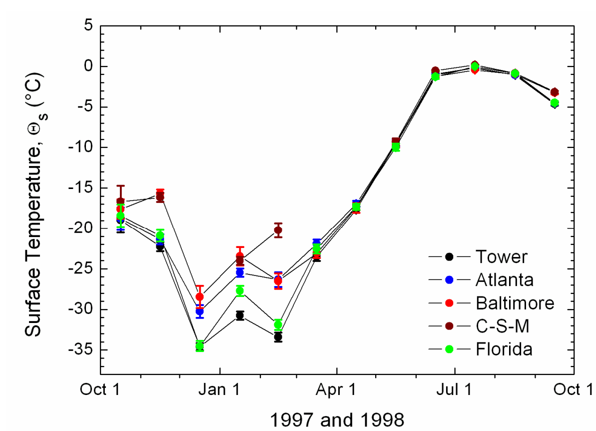

FIG. 7. As in Fig. 4 but for surface temperature (Θ_s).

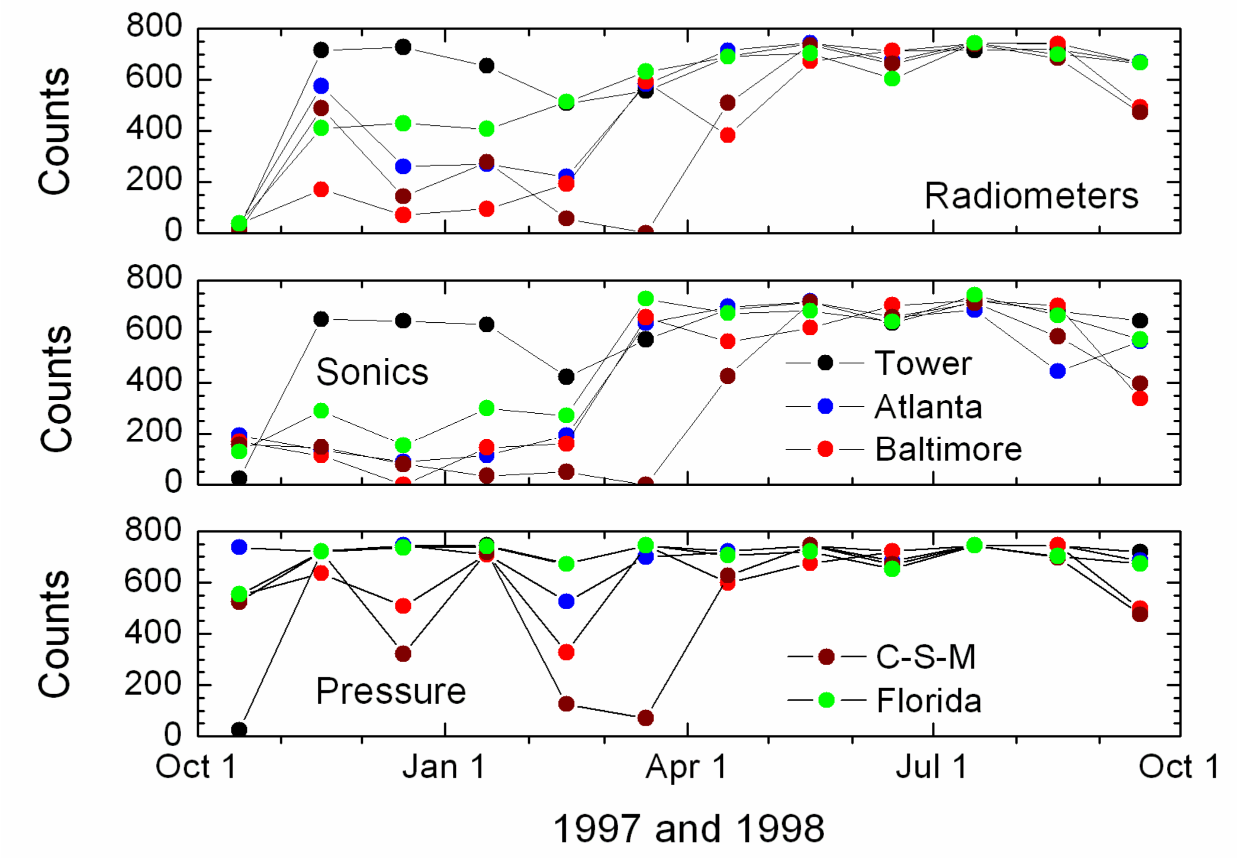

FIG. 8. Counts of the number of hours of good data for each month of SHEBA from three classes of instruments. The "Pressure" panel is typical of instruments that did not suffer icing (see Table 1): barometric pressure, air temperature, and relative humidity. The "Sonic" panel quantifies counts of good data left after screening for frosted sonics. This panel represents returns for wind speed, direction, and both the measured and bulk turbulent surface fluxes. The "Radiometer" panel represents any data streams that relied on any radiometer data: namely, both incoming and outgoing longwave and shortwave radiation, surface temperature, and the bulk turbulent surface fluxes.

points define a straight line, which has perfect positive or negative correlation.

I used the algorithms in Bendat and Piersol (1971, p. 126ff.) to evaluate 95% confidence intervals for the calculated $\rho_{V,AB}(D)$ values. These estimates suggest that we cannot have much confidence in correlation coefficients that are based on pairings for which $N_D < 15$. The following plots therefore exclude any $\rho_{V,AB}(D)$ values that resulted from fewer than 15 paired observations.

A key point to remember for interpreting these computations is that the summation in (4) includes only terms for which good measurements of variable V were available simultaneously at both sites A and B. And I use only these same data in (5) and (6). This protocol is unlike how I computed the monthly averages in the previous section, where I used all good data at a single site to compute its average.

In formulating (7), I had hypothesized that the spatial correlation function (often called the autocorrelation function; e.g., Wilks 2006, p. 58f.) of any variable in our dataset would fall off from one with increasing distance between sites (Fig. 9). This is the behavior of correlation functions computed from turbulence data that we are familiar with (e.g., Lumley and Panofsky 1964, p. 14ff.; Kaimal and Finnigan 1994, p. 33ff.; Andreas and Treviño 1997; Treviño and Andreas 2008).

As Fig. 9 depicts, if the computed spatial correlation function for variable V falls of approximately exponentially (Kaimal and Finnigan 1994, p. 35), we could characterize the spatial variability with the e-folding distance Δ such that $\rho_{V,AB}(D)$ from (7) could be represented as

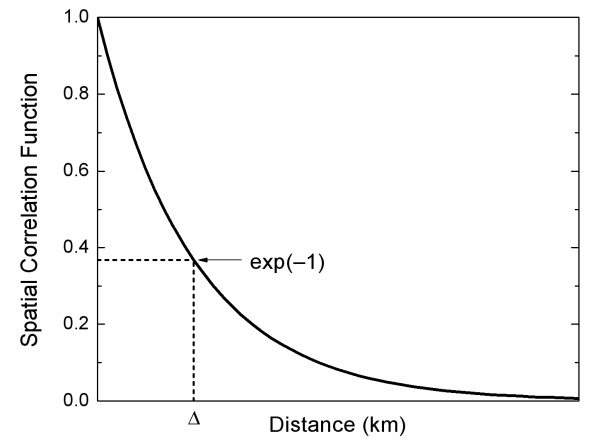

FIG. 9. Hypothesized behavior of the spatial correlation function. Quantity Δ is the e-folding distance.

$$\rho_{V,AB}(D) = \exp(-D/\Delta) . \quad (8)$$

This e-folding distance is commonly taken as the separation beyond which variables are considered uncorrelated.

4.3. Bias

Another way to evaluate the spatial variability of surface-level variables over sea ice is to calculate the bias between sites for a given variable as a function of separation.

In the same notation as above, the bias for variable V between sites A and B in a given season is

$$B_{V,AB}(D) = \frac{1}{N_D}\sum_{i=1}^{N_D}\left[V_{Ai}(P_A) - V_{Bi}(P_B)\right] . \quad (9)$$

As before, P_A is the position of site A, and P_B is the position of site B when the separation between these sites, D, is in the interval $[D_-, D_+)$. N_D is the number of simultaneous values of variable V at the two sites that have separation D during the season.

As with the correlation coefficients, for these bias calculations, I eliminated as unreliable any values that resulted from fewer than 15 paired observations. Remember, all the statistics that I will discuss are seasonal calculations; each set of paired sites could thus include over 2000 paired observations of any variable in any season (Fig. 8). Because of the screening for frost, however, some pairs early in the experiment had far fewer samples.

5. RESULTS

Although the SHEBA dataset includes simultaneous observations or calculations of 15 surface-level variables, I do not report on the four radiative components here because we already considered these elsewhere (Andreas and Jordan 2013, 2015). Here, I focus first on what are often called *state* variables—those that define the atmospheric state. Alternatively, documentation for the Community Ice Code (CICE; Hunke et al. 20013, their Table 1) identifies these variables—namely, pressure, air temperature, wind speed, and relative humidity—as quantities provided by the atmospheric model through a "flux coupler" to the sea ice model. The sea ice model, in turn, computes the final variables that I review—surface temperature and the turbulent surface fluxes—and passes them back through the flux coupler to the atmospheric model.

5.1. Pressure

As a comparative variable with nearly perfect behavior in the context of our analysis, I show in Figs. 10 and 11 the spatial correlation and bias functions for barometric pressure. Pressure gradients are generally weak over Arctic sea ice (e.g., Brown 1981); hence, the correlation coefficient is virtually one at all separations in Fig. 10. In this and all subsequent figures, the legend identifies the color scheme for the plotted points; and, in all cases, the first site listed is A, and the second site is B [see (9)].

The bias between paired sites in Fig. 11 is almost always less than 0.4 mb and has no trend with separation between sites.

5.2. Air Temperature

Andreas and Jordan (2013, 2015) show the time series of hourly 2 m air temperature (T_2) from each of the five SHEBA sites for the entire experiment (cf. Fig. 5). Temperatures started well below freezing in October 1997, fell to near −40℃ in December and January, rose slowly, and hovered around 0℃ for the three months of summer. From casual inspection, we saw that the air temperatures appear well correlated across the sites: All traces show many simultaneous peaks and valleys of short duration. Figure 12, which shows the spatial correlation functions for air temperature, confirms this result. With the exception of three insignificant outliers, the spatial correlation functions for air temperature are above 0.95 in all seasons and for all separations. No season shows the decay in correlation with separation that we hypothesized in Fig. 9.

Although the temperature bias between sites is

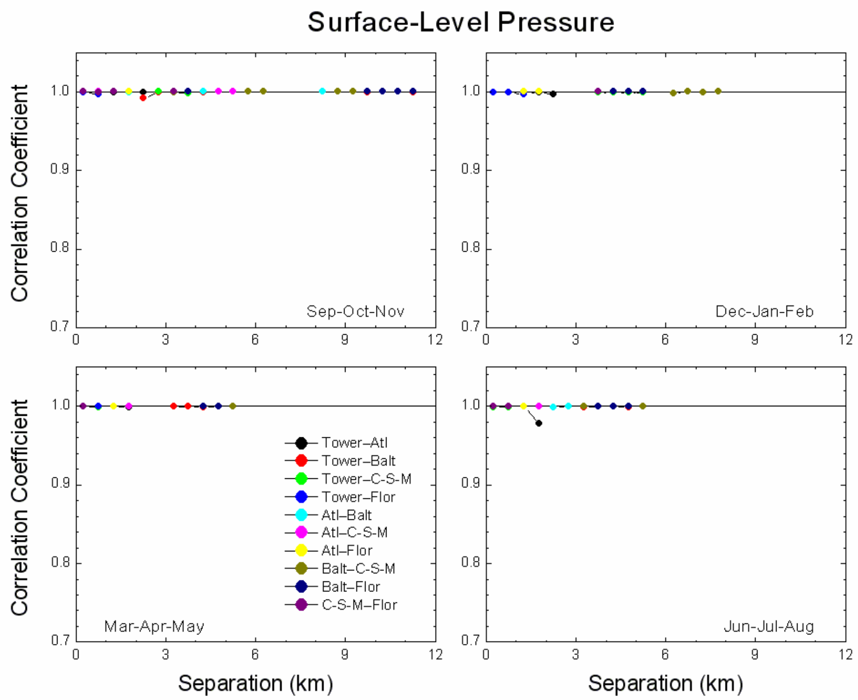

FIG. 10. The spatial correlation functions for surface-level pressure—that is, the correlation coefficient from (7) plotted as a function of separation—for the paired SHEBA sites shown in the legend. The four panels represent the usual Arctic seasons: autumn (Sep-Oct-Nov), winter (Dec-Jan-Feb), spring (Mar-Apr-May), and summer (Jun-Jul-Aug).

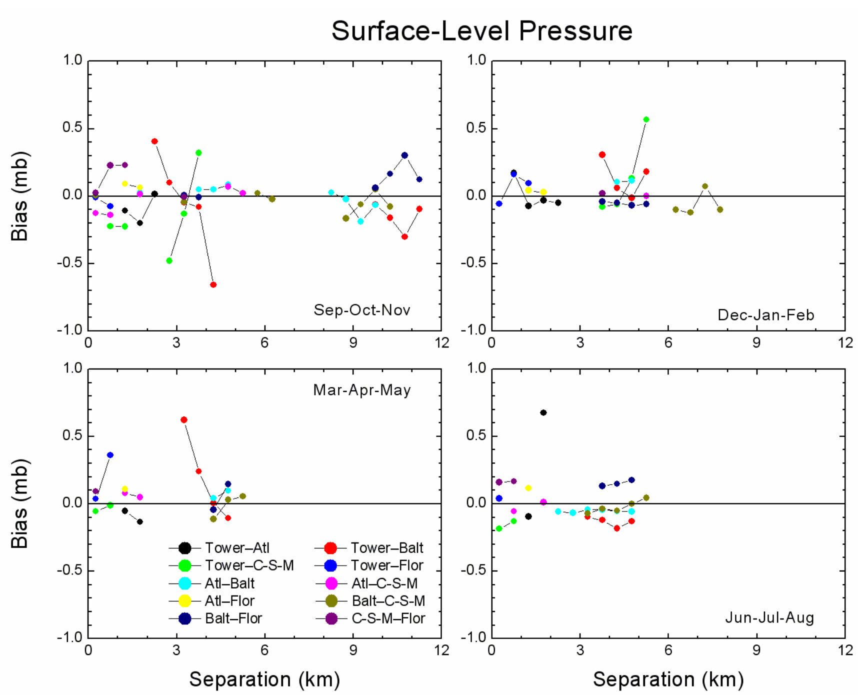

FIG 11. As in Fig. 10, but this is the bias [see (9)] for pressure as a function of separation.

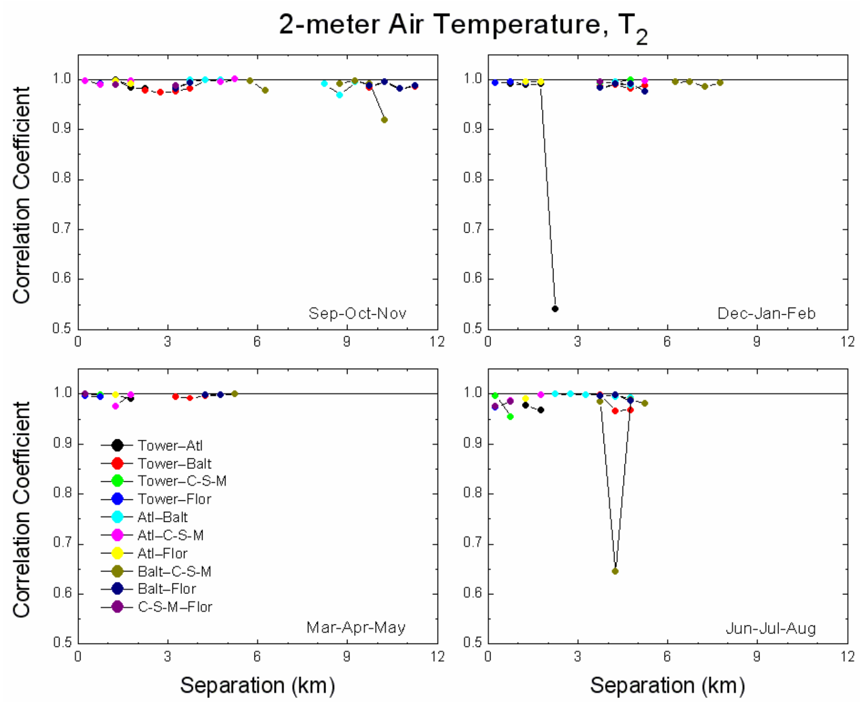

FIG. 12. As in Fig. 10, but these are the spatial correlation functions for surface-level air temperature (nominally, 2 m temperature, T_2).

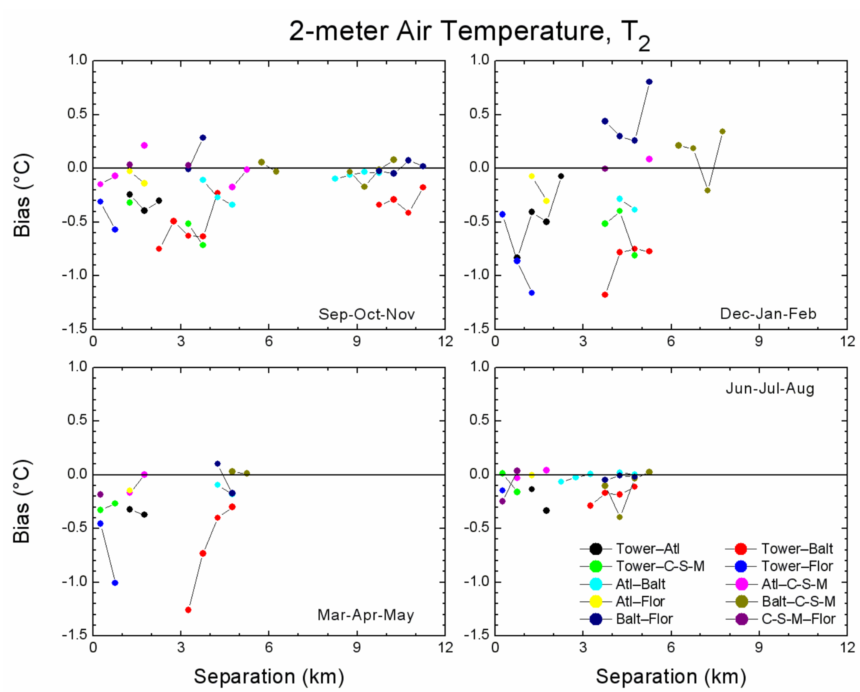

FIG. 13. As in Fig. 11, but this is the bias in air temperature between sites.

erratic in Fig. 13, the absolute value of that bias is generally less than 0.5℃. Moreover, we see at least one obvious case of instrumental bias. The red circles, representing the Tower-Baltimore pair always show a negative bias. Such consistent behavior in every season seems unlikely to have resulted from physical processes. More likely, either the Tower was biased low, the Baltimore temperature was biased high, or both.

5.3. Wind Speed

Another state variable, the surface-level wind speed (nominally at 2 m, U_2), is not as well correlated as air temperature but generally produces correlation coefficients above 0.9 (Fig. 14). And these correlation coefficients have no tendency to decrease with increasing distance between paired sites. Likewise, the bias for wind speed in Fig. 15 hovers around zero in all seasons and for all separations.

5.4. Relative Humidity

In the SHEBA dataset, surface-level relative humidity, another state variable, behaves much more erratically than air temperature and wind speed. Andreas and Jordan (2013) showed the spatial correlation functions for the SHEBA surface-level relative humidity data and concluded that inconsistent instrument response among the SHEBA relative humidity sensors explains this poor spatial coherence. After all, Andreas et al. (2002) had already demonstrated that, when figured with respect to saturation over ice, relative humidity measurements over polar sea ice all hover around 100% in all seasons.

Consequently, there is no physical reason why relative humidity should be markedly different from site to site. Rather, the seemingly erratic behavior in our plots of the statistics for relative humidity is an artifact of instrument issues (Andreas et al. 2002; Andreas and Jordan 2013). Hence, I do not show these plots but simply conclude, following Andreas et al. (2002), that relative humidity is another state variable that is well correlated for long distances over sea ice, as air temperature and wind speed are.

5.5. Surface Temperature

In a physical sense, surface temperature, Θ_s, could be a state variable; but, because in our dataset we calculated it from the incoming and outgoing longwave radiative fluxes [see (1)], it could also be considered a flux variable. In fact, starting with even the earliest models (e.g., Maykut 1978; Parkinson and Washington 1979), most sea ice models compute Θ_s by balancing the surface energy budget.

As with the other state variables, the spatial correlation functions for surface temperature are high for all separations (Fig. 16). With the exception of a few outliers, the correlation coefficients in Fig. 16 are above 0.9 in all seasons. Furthermore, those correlation functions have no trend with increasing separation.

Uncertainty assessments in Persson et al. (2002) and Andreas et al. (2010a, 2010b) place errors on individual measurements of surface temperature at ±0.5–0.6℃. Hence, the spatial bias shown in Fig. 17, which is often of order 0.5℃, is compatible with measurement uncertainties.

The winter panel (Dec-Jan-Feb) in Fig. 17 seems to have larger biases—several larger than 0.5℃—than in the other three panels. Again, these winter biases may be influenced by the poorer sampling statistics because of radiometer icing (Fig. 8).

Overland et al. (2000) presented an assessment of surface temperature that shows much more spatial variability than we found. On the basis of satellite data from an advanced very high resolution radiometer (AVHRR) collected in the vicinity of the SHEBA ice camp in December 1997 and January and February 1998, Overland et al. documented fairly broad distributions of surface temperature that tended to be skewed toward warmer surfaces. These warm tails in the AVHRR images obviously represented small fractional coverage by refrozen leads.

In placing our SHEBA ASFG sites, we admittedly avoided thin ice in refrozen leads because we wanted the sites to survive. Consequently, all of our sites, except Baltimore, were preferentially on thicker ice where we were likely to see only small differences in surface temperature between sites.

Baltimore, however, was intentionally placed on a refrozen polynya where the ice was 0.4 m thick at the time of deployment. And this thin-ice site does seem to corroborate the observations by Overland et al. (2000). In Fig. 17, in autumn and winter, the surface temperature at Baltimore is consistently higher than at the multiyear ice sites: the tower, Atlanta, and Florida. In other words, in the autumn and winter panels in Fig. 17, the “Tower-Balt” and “Atl-Balt” points are negative while the “Balt-Flor” points are positive. In each sequence, Baltimore has the higher seasonal surface temperature.

These biases fade to near zero in spring and summer. In spring, the ice at all sites has thickened and, thereby, minimized surface heating from the warmer ocean. In summer, the entire near-surface environment is tending to 0℃. The same biases that we saw in October through February return in

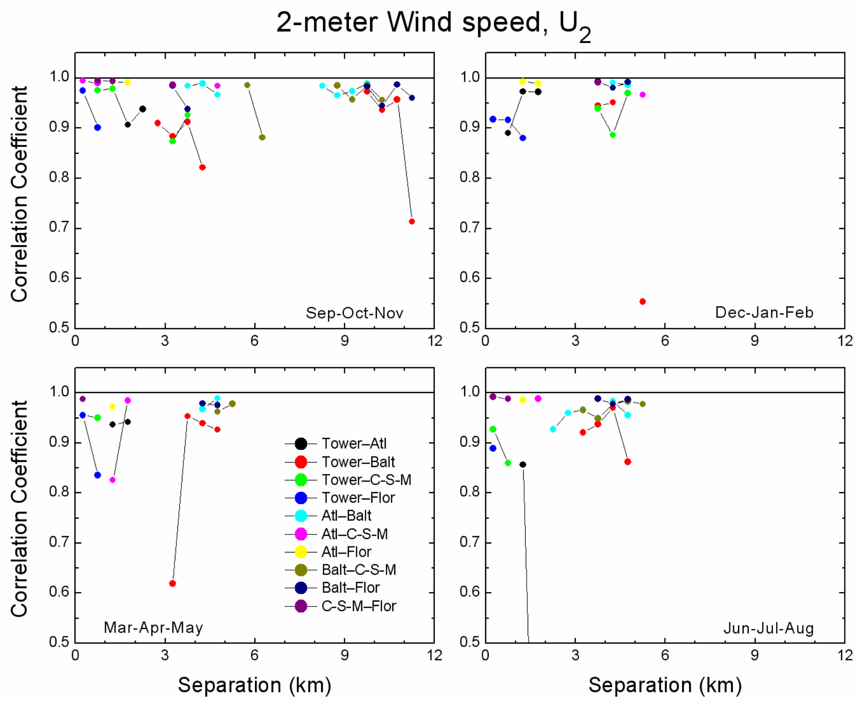

FIG. 14. As in Fig. 10, but these are the spatial correlation functions for surface-level wind speed (nominally at 2 m, U_2).

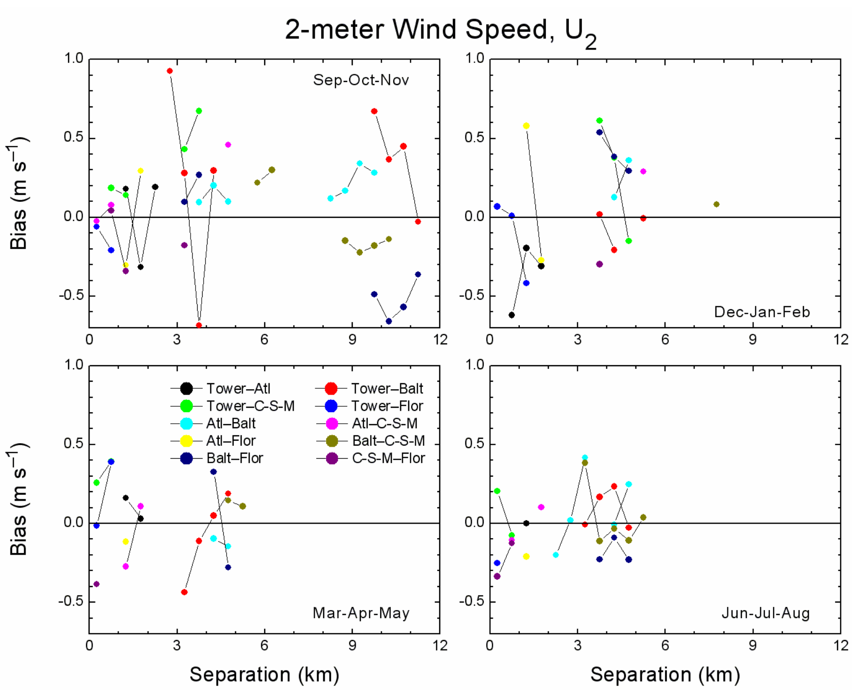

FIG. 15. As in Fig. 11, but this is the bias in wind speed between sites.

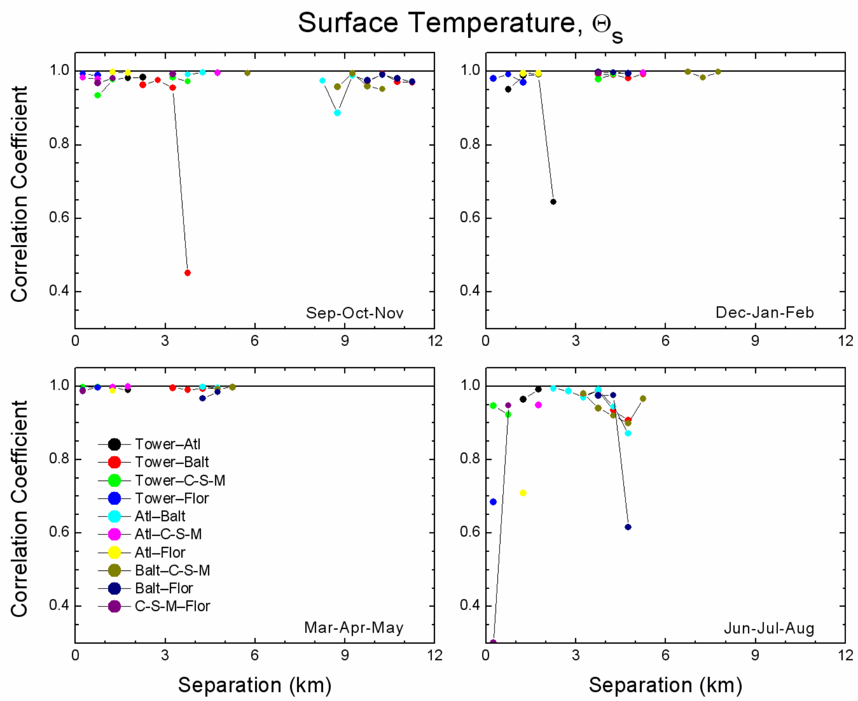

FIG. 16. As in Fig. 10, but these are the spatial correlation functions for surface temperature, Θ_s, which I calculated from (1).

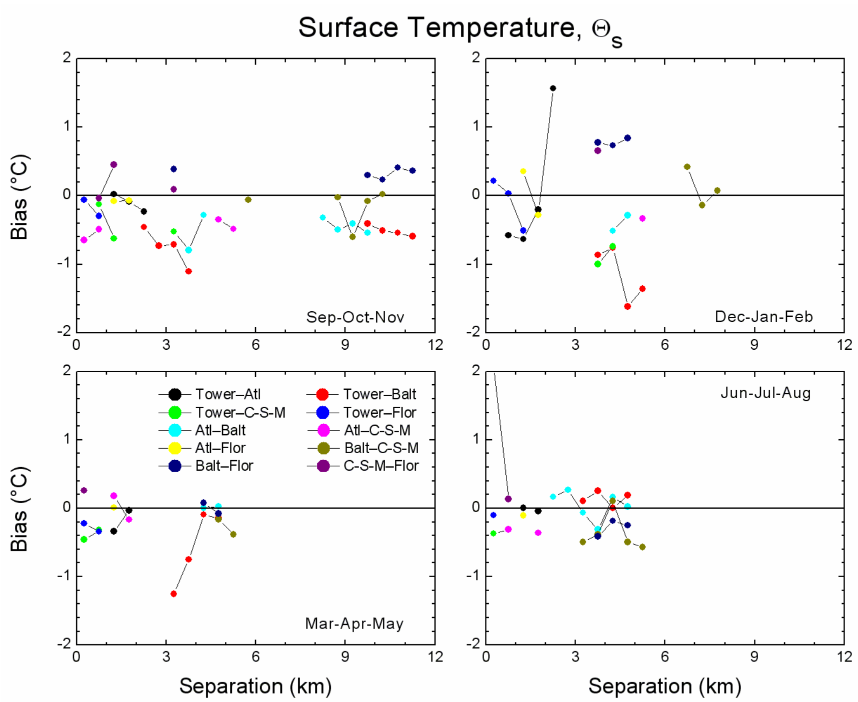

FIG. 17. As in Fig. 10, but this is the spatial bias for surface temperature.

September 1998, however, when Baltimore still features the thinnest ice.

Haggerty et al. (2003) also studied the variability in surface temperature around the SHEBA camp, but their measurements were from an aircraft in spring (May 1998) and summer (July 1998). As in our analysis, Haggerty et al. found neither spring nor summer showed marked spatial variability in surface temperature; standard deviations in surface temperature during various flight legs were typically 0.5°C, as were our bias values in Fig. 17. In both months, however, open and refreezing leads stood out as being significantly warmer than the sea ice, which, of course, was not warmer than 0°C. We did not adequately measure surface temperatures of leads at any or our sites.

5.6. Turbulent Surface Fluxes

I next consider the turbulent surface fluxes of momentum (τ) and sensible (H_s) heat. Because I report here both the measured fluxes and the fluxes computed from a bulk flux algorithm, I need to briefly describe that algorithm.

The turbulent fluxes and their parameterizations generally take the form (e.g., Fairall et al. 1996, 2003; Andreas et al. 2010a, 2010b)

$$\tau = -\rho\overline{uw} = \rho u_*^2 = \rho C_{Dr} S_r^2 , \qquad (10a)$$

$$H_s = \rho c_p \overline{w\theta} = \rho c_p C_{Hr} S_r (\Theta_s - \Theta_r) , \qquad (10b)$$

$$H_L = \rho L_v \overline{wq} = \rho L_v C_{Er} S_r (Q_s - Q_r) . \qquad (10c)$$

Here, u, w, θ, and q are, respectively, the turbulent fluctuations in the along-wind velocity, vertical velocity, air temperature, and specific humidity. The overbars denote time averages; hence, $\overline{uw}$, $\overline{w\theta}$, and $\overline{wq}$ indicate how we measured the momentum flux, sensible heat flux, and latent heat flux (H_L). S_r, Θ_r, and Q_r are average effective wind speed, potential temperature, and specific humidity at reference height r; Θ_s is again the surface temperature; and Q_s is the specific humidity at the surface, which I evaluated as the saturation value at Θ_s. The ρ, c_p, and L_v are the air density, the specific heat of air at constant pressure, and the latent heat of vaporization or sublimation. Equation (10a) also defines the friction velocity, u_*.

From measurements of $\overline{uw}$, $\overline{w\theta}$, $\overline{wq}$, S_r, Θ_r, Q_r, and Θ_s, Andreas et al. (2010a, 2010b) developed parameterizations for the turbulent transfer coefficients C_{Dr} (the drag coefficient appropriate for height r), C_{Hr}, and C_{Er} (the scalar transfer coefficients for height r).

In a model or a standalone analysis, the right sides of (10) are solved iteratively to compute the fluxes. Other equations in this iteration are the parameterizations for C_{Dr}, C_{Hr}, and C_{Er} and an equation for the Obukhov length, L, on which the transfer coefficients depend. This is

$$L = -\left[\frac{kg}{\overline{T}u_*^3}\left(\frac{H_s}{\rho c_p} + \frac{0.61\overline{T}}{1+0.61\overline{Q}}\frac{H_L}{\rho L_v}\right)\right]^{-1} . \qquad (11)$$

Here, g is the acceleration of gravity; k (= 0.40), the von Kármán constant; and $\overline{T}$ and $\overline{Q}$, average air temperature and specific humidity in the near-surface layer.

Using the bulk flux algorithms for summer and winter sea ice reported in Andreas et al. (2010a, 2010b; available in Fortran at www.nwra.com/resumes/andreas/software.php), I iteratively solved (10) and (11) for every hour at every SHEBA site that had adequate forcing data for the hour. In the discussion to follow, I use u_* as a surrogate for both the measured and modeled momentum flux.

Figure 18 shows the spatial correlation functions for the measured u_*; Fig. 19 is the associated plot of spatial bias for the measured u_*.

Both plots have different character than the previous plots of correlation and bias. The scatter in these figures is much wider because u_* is a turbulence variable measured by eddy-covariance. Measured turbulent fluxes are known to have a typical minimum uncertainty of about ±10% for u_* and ±20% for H_s and H_L (e.g., Fairall et al. 1996; Finkelstein and Sims 2001; Andreas et al. 2010b). This minimum uncertainty is usually associated with random error (e.g., Vickers and Mahrt 1997; Mahrt 2010); Finkelstein and Sims (2001) term this uncertainty the sampling error. Quite simply, the turbulent fluctuations u, w, θ, and q are random variables; covariances formed from them have inherent randomness among measuring sites even if the surface is horizontally homogeneous.

Both the bias and correlation also suffer from sensor icing of the Flux-PAM sonic anemometers from October 1997 to almost the end of February 1998, when we fitted heaters to the sonic arms and established a heating protocol. Unlike the radiometers, however, the PAM sonics flagged data when icing was occurring; hence, I rejected those data in my calculations of u_* and H_s. Icing episodes, however, did reduce the number of good hourly measurements for use in the analysis. These smaller numbers of samples increased the uncertainty in the correlation coefficients and in the biases as evidenced by the larger scatter in both Figs.

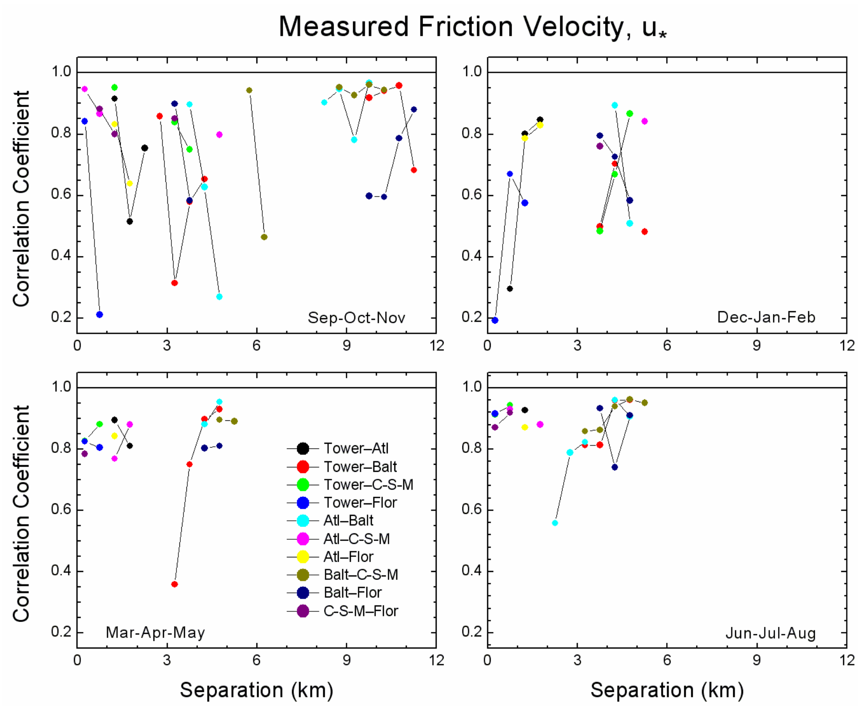

FIG. 18. As in Fig. 10, but this figure shows the spatial correlation functions for the measured friction velocity, u_*; see (10a).

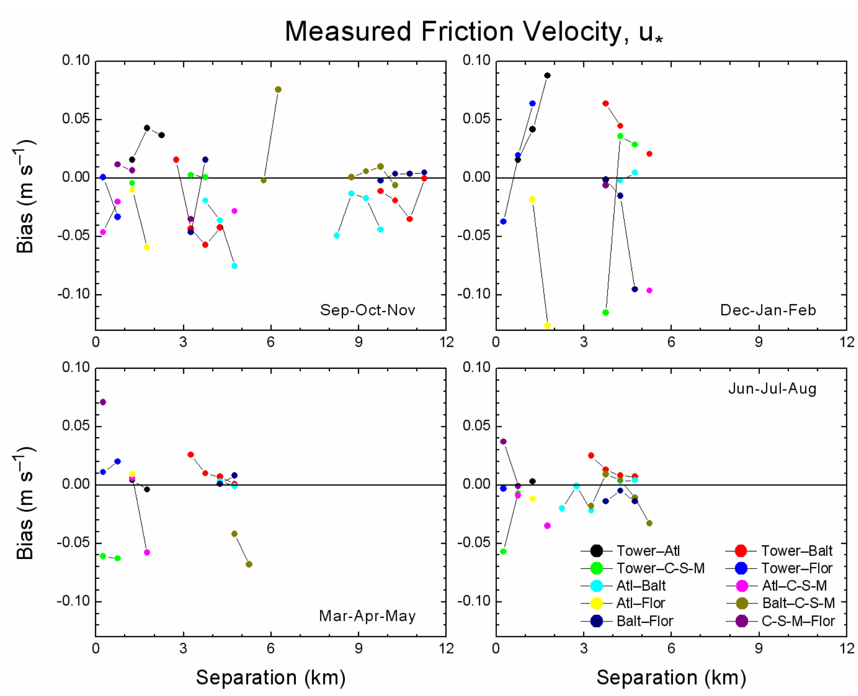

FIG. 19. As in Fig. 11, but this is the bias in the measured friction velocity.

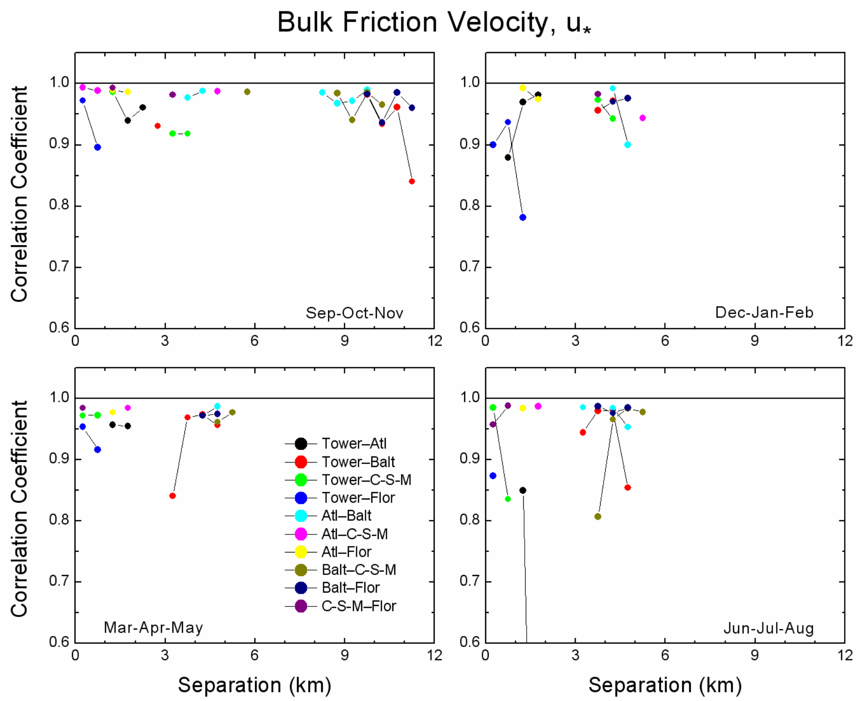

FIG. 20. As in Fig. 18, but these are the spatial correlation functions for the friction velocity computed from the bulk flux algorithm.

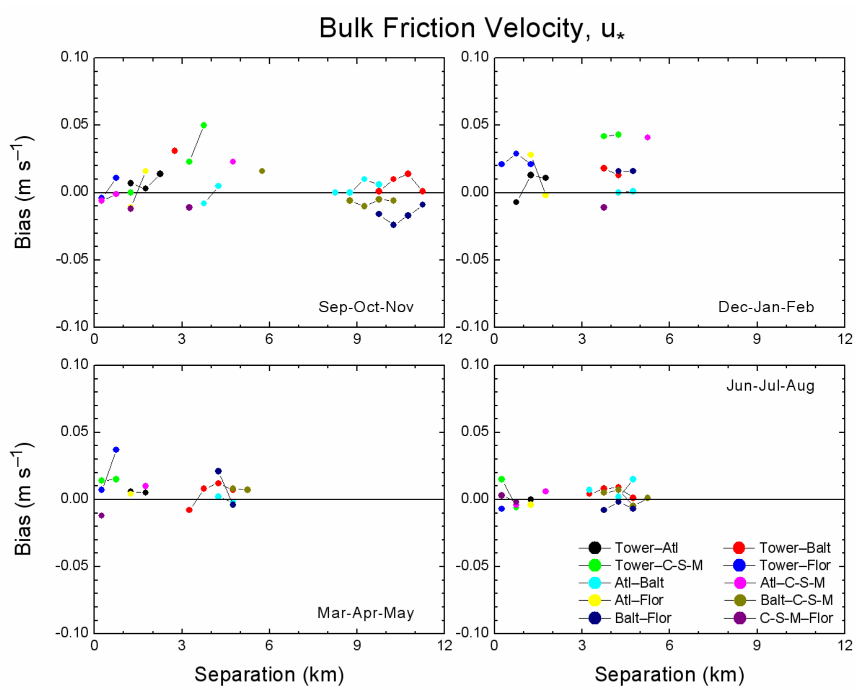

FIG. 21. As in Fig. 19, but this is the spatial bias for the bulk friction velocity.

18 and 19 for October through February 1998.

The best quality data in Fig. 18—the September 1998 data from Baltimore and the spring and summer panels—suggest that the correlation coefficient for measured friction velocity was typically above 0.8 and had no tendency to decrease with increasing separation. The same best quality data in the bias plot, Fig. 19, suggest a fairly small bias in measured u_* between sites—almost always less than 0.05 m s^{-1} (5 cm s^{-1})—and, as usual, no tendency to change with separation.

As companions to Figs. 18 and 19, I show in Figs. 20 and 21 the spatial correlation functions and the spatial bias for the bulk friction velocity that results from running the Andreas et al. (2010a, 2010b) bulk flux algorithm for each SHEBA site. This bulk friction velocity is analogous to what a numerical model would produce when it computes flux boundary conditions and, therefore, is probably more relevant to interpreting the assumption of grid cell uniformity than is the previous analysis of measured friction velocity.

Both Figs. 20 and 21 are in sharp contrast to Figs. 18 and 19. In Fig. 20, the correlation coefficient is almost always greater than 0.90 in all seasons; and in Fig. 21, the bias in the bulk u_* is always less than $\pm$0.05 m s^{-1} and usually less than $\pm$0.02 m s^{-1}. I attribute this better behavior in the bulk friction velocity than in the measured friction velocity to how I obtained the bulk u_*. It derived from the mean meteorological variables wind speed, temperature, humidity, and surface temperature through (10) and (11). Because I have already established with Figs. 12, 14, and 16 that these variables are highly correlated, quantities computed from them should be also.

The spatial correlation functions for the measured sensible heat flux, H_s, in Fig. 22 are even more wild than for the measured friction velocity. Again, H_s is a turbulence variable that has inherent random scatter; but, to compound matters over sea ice, the sensible heat flux is generally small in all seasons. Andreas et al. (2010a, 2010b) showed that, during SHEBA, measured hourly values of the sensible heat flux were mostly between –20 and +20 W m^{-2} (cf. Persson et al. 2002; Brunke et al. 2006). With small values common and uncertainty in any individual measurement large, one site in the correlation analysis could show a positive heat flux for a given hour while another site could show a negative flux. Pairing these data obviously degrades the correlation coefficient.

As in Fig. 18, the October 1997 through February 1998 data in Fig. 22 suffer also from icing of the PAM sonics. This period clearly produces the poorest correlation coefficients in Fig. 22. The spring and summer panels and the September 1998 data from Baltimore in Fig. 22, which do not reflect instrument problems, generally have higher correlation coefficients.

The small sensible heat fluxes do lead to small biases in Fig. 23. The winter (Dec-Jan-Feb) panel in Fig. 23 has the most erratic biases; I again attribute these to data sparsity resulting from icing of the PAM sonics. The other panels in Fig. 23 depict biases that are generally within 5 W m^{-2} of zero. We see no evidence of any dependence on separation in the biases in Fig. 23.

As with the bulk friction velocity, the surface sensible heat fluxes that I computed with the bulk flux algorithm are more comparable to what a weather or climate model would simulate than are the measured fluxes in Figs. 22 and 23. Figures 24 and 25 therefore show the spatial correlation functions and the bias for the bulk sensible heat flux.

In contrast to the bulk friction velocity, for which the spatial correlation functions (Fig. 20) were better behaved than for the measured friction velocity (Fig. 18), the spatial correlation functions for the bulk sensible heat flux in Fig. 24 have scatter similar to the correlation function for measured sensible heat flux (Fig. 22). I again attribute this behavior to the generally small heat fluxes in all seasons and the associated small surface-air temperature difference [i.e., $\Theta_s - \Theta_r$ in (10b)] that drives the sensible heat flux in the bulk flux algorithm. That is, with the inherent uncertainty in Θ_s of $\pm$0.5°C, when $\Theta_s - \Theta_r$ is small, $\Theta_s - \Theta_r$ could be measured as slightly positive at one site but slightly negative at another site. The computed sensible heat fluxes would then have opposite signs, and the correlation between the sites would degrade.

On the other hand, the bias in bulk sensible heat flux that Fig. 25 depicts is similar to what we saw with the measured sensible heat flux in Fig. 23. Again, the bias in Fig. 25 is small because all of the sensible heat fluxes are small in all seasons: The difference between two small numbers is always a small number.

Because we had only one measurement of latent heat flux at SHEBA—at one level on the main 20 m tower—I cannot assess the spatial variability of the measured latent heat flux. Nevertheless, I could still compute the bulk latent heat flux at each SHEBA site for the hours with sufficient forcing data. Figures 26 and 27 show the spatial correlation functions and the bias for the bulk latent heat flux.

These two plots have characteristics similar to the comparable plots for the bulk sensible heat flux: The correlation functions can be pretty wild, but the biases are small. I see no dependence on separation in either plot.

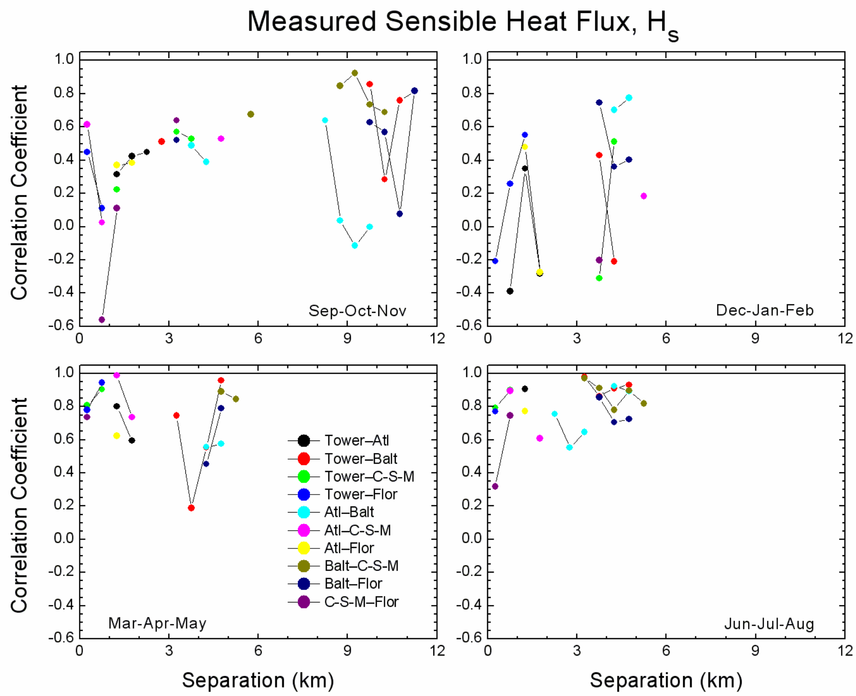

FIG. 22. As in Fig. 10, but these are the spatial correlation functions for the measured sensible heat flux, H_s; see (10b).

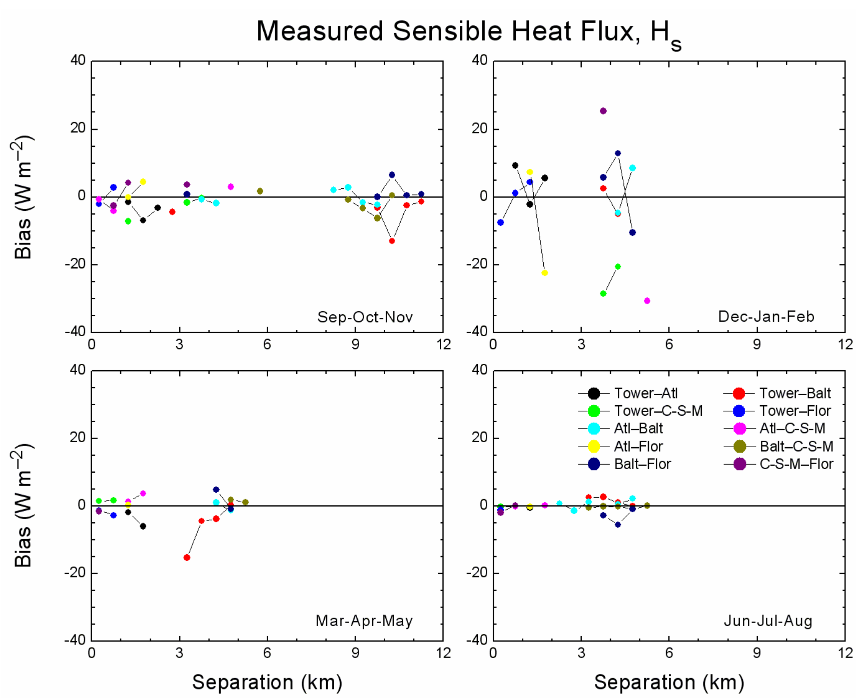

FIG. 23. As in Fig. 11, but this shows the spatial bias in measured sensible heat flux.

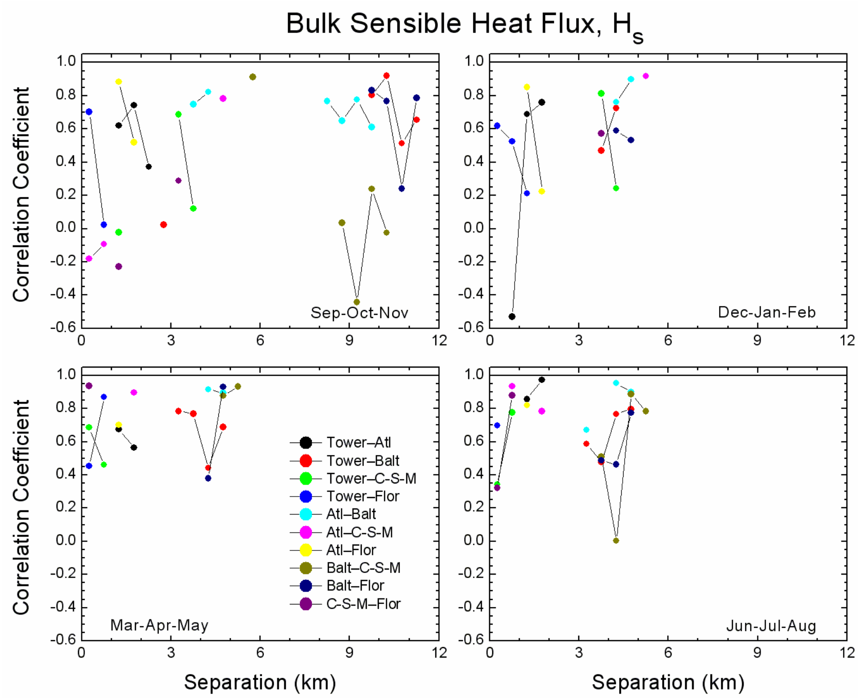

FIG. 24. As in Fig. 22, but these are the spatial correlation functions for the bulk sensible heat flux computed from the bulk flux algorithm, (10) and (11).

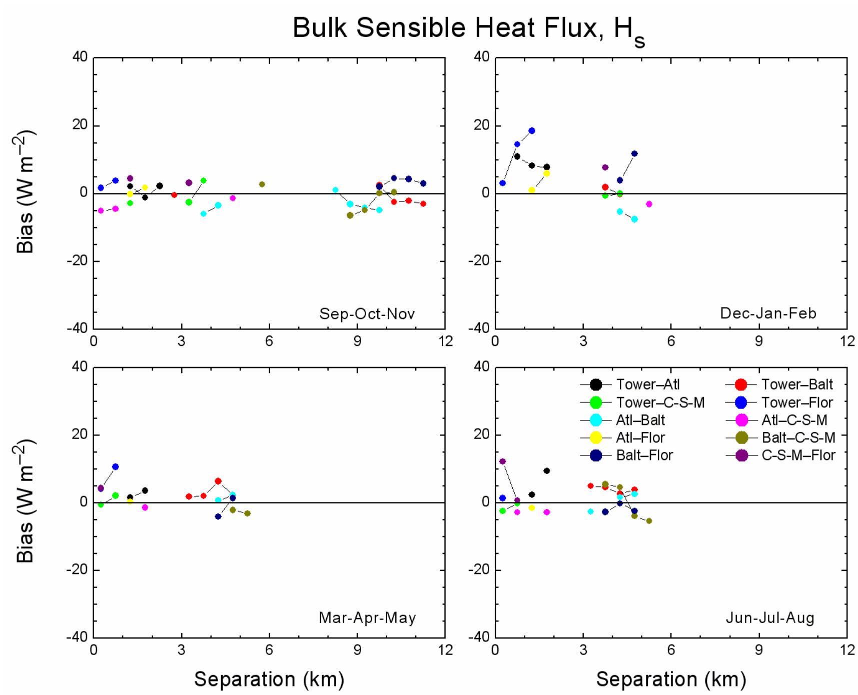

FIG. 25. As in Fig. 23, but this is the spatial bias for the surface sensible heat flux from the bulk flux algorithm.

If anything, the bulk latent heat flux panels in Fig. 26 may show slightly better correlation than the panels for bulk sensible heat flux do. (Notice the difference in vertical scales in Figs. 24 and 26.) I speculate that this better correlation may result because, at SHEBA, the latent heat flux tended to be mostly positive while the sensible heat flux was more evenly distributed between positive and negative fluxes (Andreas et al. 2013). That is, in the correlation calculations, a positive sensible heat flux at one site might be frequently paired with a negative flux at another site. Such a pairing would degrade the correlation. For the latent heat flux, in contrast, positive-positive pairings would be more common.

The biases in bulk latent heat flux in Fig. 27 are typically less than about 2 W m^{-2} in magnitude. These small biases simply reflect the small magnitude of the latent heat flux over sea ice, where the magnitude of the latent heat flux is generally reported to be smaller than 10 W m^{-2} in all seasons (e.g., Persson et al. 2002; Andreas et al. 2010a, 2010b).

6. DISCUSSION AND CONCLUSIONS

This analysis of 11 different surface-level meteorological variables obtained from a year of SHEBA data generally supports the assumption of uniformity in these variables over model grid cells up to 12 km across. The variables that I analyzed were barometric pressure; surface-level (i.e., ~2 m) air temperature, wind speed, and relative humidity; surface temperature; and both the measured and bulk turbulent surface fluxes.

I computed three metrics to judge the spatial variability of these variables: the monthly average and seasonal values of the spatial correlation function (7) and the spatial bias (9). Especially in spring, summer, and early autumn, when we had the most complete data returns, the monthly averages hinted at the uniformity in conditions. In plots of the seasonal metrics as functions of separation between sites in each of the four Arctic seasons—autumn, winter, spring, and summer—I saw no obvious degradation in any of the functions as the separation between sites increased, contrary to my original hypothesis (i.e., Fig. 9). All seasons included results for separations up to 6 km. The calculations for autumn had separations up to 12 km.

Admittedly, our selections for the five SHEBA sites could have affected these conclusions. We deployed all five original sites on fairly thick ice. Site Baltimore started on the thinnest ice, a refrozen polynya that had ice 0.4 m thick in autumn 1997. These choices certainly affected the range in surface temperatures that we measured, especially in winter when thin ice has a warmer surface than thicker ice (e.g., Overland et al. 2000).

From this bias in our sites toward thicker ice and from recognizing the known increase in surface temperature over thinner ice in winter (Makshtas 1991, p. 32ff.; Overland et al. 2000), I conclude that—at least in winter—accounting for the range in surface temperature over a model grid cell as a function of ice thickness will be necessary (e.g., Thorndike 1992; Hunke and Bitz 2009). Most modern sea ice models recognize this fact and include a distribution of ice thicknesses within a single grid cell (e.g., Bitz et al. 2001; Lipscomb 2001; Lindsay 2003; Holland et al. 2006). The turbulent sensible and latent heat fluxes, which respond to surface temperature, may also need to be evaluated as functions of ice thickness (e.g., Lindsay 2003). The emitted longwave radiation may also vary with ice thickness because it goes as the fourth power of the surface temperature.

In late spring and summer, on the other hand, when the surface ocean, the sea ice, and the air all tend to 0°C, spatial uniformity in surface temperature is a better assumption. Of course, Haggerty et al. (2003) did find significantly higher surface temperatures in leads than for the surrounding ice during aircraft flights in May and July of the SHEBA year. The May observations found that the ice was still relatively cool compared to the open water or new ice in leads. During the July observations, the leads were slightly above freezing from solar heating while the sea ice was near freezing. This heated surface layer may not have existed, however, if the wind mixing had been stronger (cf. Paulson and Pegau 2001). Still, even during the melting season, treating leads individually within a grid cell may be necessary.

We could place no instruments over open water, like leads or polynyas, although our instruments did adequately sample over melt ponds during the summer. Conceivably, the 2 m air temperature could be higher over open ocean water than over compact sea ice, at least in winter. Hence, again, significant differences in surface-level air temperature could exist over a model grid cell. But observations of Arctic leads suggest that, even in winter, the heating from the water surface does not reach very far above that surface: The heat is all blown downwind. Andreas et al. (1979) show temperature profiles measured over wintertime leads with widths up to 85 m. In all of these, the temperature at 2 m is within a few tenths of a degree Celsius of the temperature of the upwind air over compact sea ice despite the fact that the leads were 20°–25°C warmer than the upwind ice. Makshtas (1991, p. 34f.) made the same observations over a polynya that was up to 119 m wide. In other words, the 2 m air temperature can be

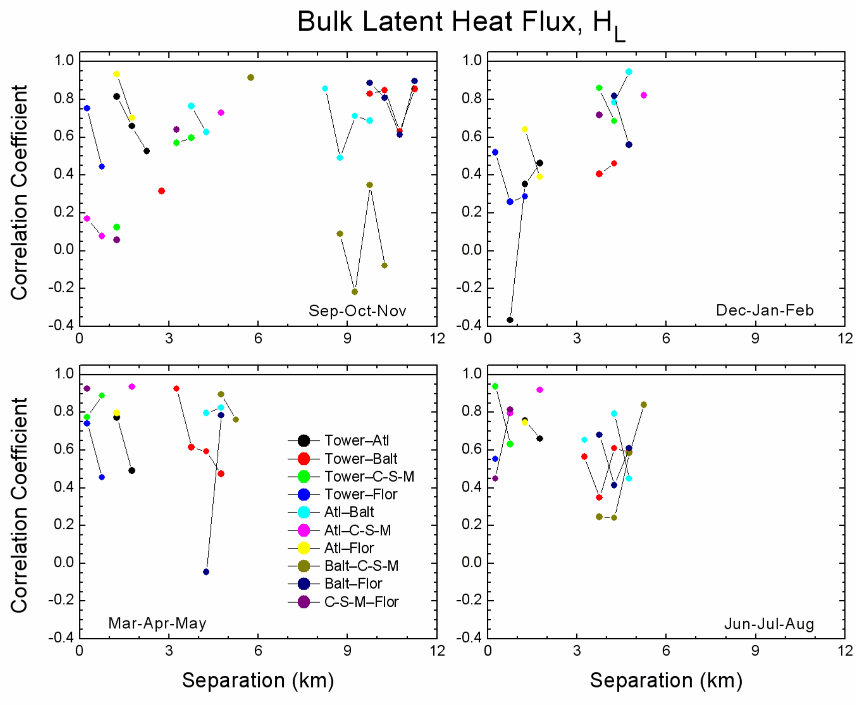

FIG. 26. As in Fig. 24, but these are the spatial correlation functions for the bulk latent heat flux computed from the bulk flux algorithm, (10) and (11).

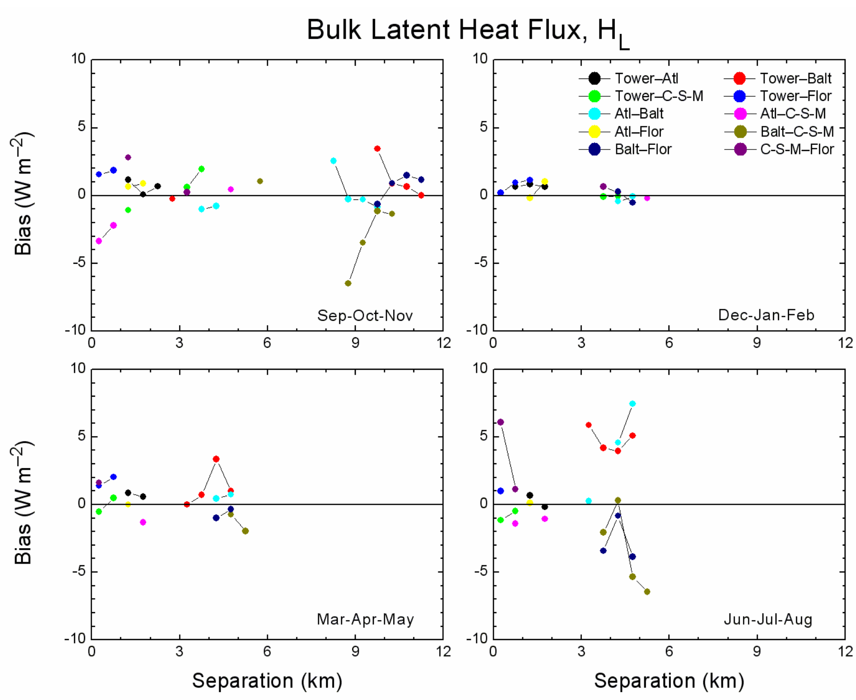

FIG. 27. As in Fig. 25, but this shows the spatial bias for the bulk latent heat flux computed from the bulk flux algorithm.

assumed homogeneous over grid cells up to 12 km, even if the grid cell contains open water. The higher surface temperature and lower albedo of the open water must, nevertheless, still be accounted for in the radiative fluxes and in the turbulent heat fluxes.

The surface-level wind speed is similarly well mixed 2 m above the surface in all seasons whether the surface is water or ice.

In summary, this analysis justifies the assumption that, over the central Arctic ice pack, the variables surface-level pressure, air temperature, wind speed, and humidity are uniform over model grid cells up to 12 km.

In the cold season, the surface temperature is not uniform over grid cells that include open water or a range of ice thicknesses. Conduction through the ice from the relatively warm surface ocean affects the surface temperature of the bare ice. Even a small amount of snow cover, however, will homogenize these surface temperatures because conduction through snow is much slower. Any variable that responds strongly to surface temperature—like emitted longwave radiation and surface sensible and latent heat fluxes—may, therefore, also be heterogeneous over grid cells that include both thin and thicker ice and a variety of snow depths.

In summer, our data show little evidence of spatial variability in surface temperature. Aircraft observations during the SHEBA summer (Haggerty et al. 2003) that could adequately sample leads, do suggest surface temperatures in this open water that are 1–2°C above freezing (also Paulson and Pegau 2001). Again, variables that are sensitive to surface temperature may need to be treated as heterogeneous over model grid cells in summer.

In the end, some readers may view this analysis as weakly relevant since Arctic sea ice is thinner in winter and open water is more prevalent in summer now than during the SHEBA year. But remember, climate simulations, for instance, require a spin up of several centuries (e.g., Collins et al. 2006; Hurrell et al. 2013) before they can accurately simulate current conditions or predict future climate. My analysis is certainly pertinent to these several hundred years before present.

7. ACKNOWLEDGMENTS

I thank my colleagues in the SHEBA Atmospheric Surface Flux Group, who helped collect, process, and interpret the SHEBA data: Chris Fairall, Andrey Grachev, Peter Guest, Tom Horst, and Ola Persson. I also thank Rachel Jordan for valuable discussions on this work, John Weatherly for reviewing an early draft of the manuscript, and Emily Moynihan of BlytheVisual for creating Fig. 2. The U.S. National Science Foundation supported this work with award ARC 10-19322; the Office of Naval Research, with award N00014-12-C-0290.

8. REFERENCES

Andreas, E. L, and R. E. Jordan, 2013: Spatial correlation of surface-level variables over Arctic sea ice. *Extended abstracts, 12th Conf. on Polar Meteorology and Oceanography*, Seattle, WA, Amer. Meteor. Soc., paper 5.3, 14 pp.

____, and ____, 2015: Spatial variability of surface-level variables over Arctic sea ice. *J. Climate*, submitted.

____, and G. Treviño, 1997: Using wavelets to detect trends. *J. Atmos. Oceanic Technol.*, **14,** 554–564.

____, C. A. Paulson, R. M. Williams, R. W. Lindsay, and J. A. Businger, 1979: The turbulent heat flux from Arctic leads. *Bound.-Layer Meteor.*, **17,** 57–91.

____, C. W. Fairall, P. S. Guest, and P. O. G. Persson, 1999: An overview of the SHEBA atmospheric surface flux program. Preprints, *Fifth Conf. on Polar Meteorology and Oceanography*, Dallas, TX, Amer. Meteor. Soc., 411–416.

____, P. S. Guest, P. O. G. Persson, C. W. Fairall, T. W. Horst, R. E. Moritz, and S. R. Semmer, 2002: Near-surface water vapor over polar sea ice is always near ice saturation. *J. Geophys. Res.*, **107,** 8032, doi:10.1029/2000JC000411.

____, T. W. Horst, A. A. Grachev, P. O. G. Persson, C. W. Fairall, P. S. Guest, and R. E. Jordan, 2010a: Parameterising turbulent exchange over summer sea ice and the marginal ice zone. *Quart. J. Roy. Meteor. Soc.*, **136,** 927–943.

____, P. O. G. Persson, R. E. Jordan, T. W. Horst, P. S. Guest, A. A. Grachev, and C. W. Fairall, 2010b: Parameterizing turbulent exchange over sea ice in winter. *J. Hydrometeor.*, **11,** 87–104.

____, R. E. Jordan, L. Mahrt, and D. Vickers, 2013: Estimating the Bowen ratio over the open and ice-covered ocean. *J. Geophys. Res. Oceans*, **118,** 4334–4345, doi:10.1002/jgrc.20295.

Bendat, J. S., and A. G. Piersol, 1971: *Random Data: Analysis and Measurement Procedures*. Wiley-Interscience, 407 pp.

Bitz, C. M., and W. H. Lipscomb, 1999: An energy-conserving thermodynamic model of sea ice. *J. Geophys. Res.*, **104,** 15,669–15,677.

____, M. M. Holland, A. J. Weaver, and M. Eby, 2001: Simulating the ice-thickness distribution in a coupled climate model. *J. Geophys. Res.*, **106,** 2441–2463.

Bromwich, D. H., K. M. Hines, and L.-S. Bai, 2009:

Development and testing of Polar Weather Research and Forecasting model: 2. Arctic Ocean. *J. Geophys. Res.*, **114,** D08122, doi:10.1029/2008JD010300.

Brown, R. A., 1981: Modeling the geostrophic drag coefficient for AIDJEX. *J. Geophys. Res.*, **86,** 1989–1994.

Brun, E., Z.-L. Yang, R. Essery, and J. Cohen, 2008: Snow-cover parameterization and modeling. *Snow and Climate: Physical Processes, Surface Energy Exchange and Modeling*, R. L. Armstrong and E. Brun, Eds., Cambridge University Press, 125–180.

Brunke, M. A., M. Zhou, X. Zeng, and E. L Andreas, 2006: An intercomparison of bulk aerodynamic algorithms used over sea ice with data from the SHEBA experiment. *J. Geophys. Res.*, **111,** C09001, doi:10.1029/2005JC002907.

Chung, Y.-C., S. Bélair, and J. Mailhot, 2011: Blowing snow on Arctic sea ice: Results from an improved sea ice-snow-blowing snow coupled system. *J. Hydrometeor.*, **12,** 678–689.

Collins, W. D., and Coauthors, 2006: The Community Climate System Model Version 3 (CCSM3). *J. Climate*, **19,** 2122–2143.

Fairall, C. W., E. F. Bradley, D. P. Rogers, J. B. Edson, and G. S. Young, 1996: Bulk parameterization of air-sea fluxes for Tropical Ocean-Global Atmosphere Coupled-Ocean Atmosphere Response Experiment. *J. Geophys. Res.*, **101,** 3747–3764.

____, ____, J. E. Hare, A. A. Grachev, and J. B. Edson, 2003: Bulk parameterization of air-sea fluxes: Updates and verification for the COARE algorithm. *J. Climate*, **16,** 571–591.

Finkelstein, P. L., and P. F. Sims, 2001: Sampling errors in eddy correlation flux measurements. *J. Geophys. Res.*, **106,** 3503–3509.

Grachev, A. A., C. W. Fairall, P. O. G. Persson, E. L Andreas, and P. S. Guest, 2005: Stable boundary-layer scaling regimes: The SHEBA data. *Bound.-Layer Meteor.*, **116,** 201–235.

____, E. L Andreas, C. W. Fairall, P. S. Guest, and P. O. G. Persson, 2007: SHEBA flux-profile relationships in the stable atmospheric boundary layer. *Bound.-Layer Meteor.*, **124,** 315–333.

Haggerty, J. A., J. A. Maslanik, and J. A. Curry, 2003: Heterogeneity of sea ice surface temperature at SHEBA from aircraft measurements. *J. Geophys. Res.*, **108,** 8052, doi:10.1029/2000JC000560.

Holland, M. M., 2003: An improved single-column model representation of ocean mixing associated with summertime leads: Results from a SHEBA case study. *J. Geophys. Res.*, **108,** 3107, doi:10.1029/2002JC001557.

____, C. M. Bitz, E. C. Hunke, W. H. Lipscomb, and J. L. Schramm, 2006: Influence of sea ice thickness distribution on polar climate in CCSM3. *J. Climate*, **19,** 2398–2414.

Horst, T. W., S. P. Oncley, and S. R. Semmer, 1997: Measurement of water vapor fluxes using capacitance RH sensors and cospectral similarity. Preprints, *12th Symp. on Boundary Layers and Turbulence*, Vancouver, B.C., Amer. Meteor. Soc., 360–361.

Hunke, E. C., and C. M. Bitz, 2009: Age characteristics in a multidecadal Arctic sea ice simulation. *J. Geophys. Res.*, **114,** C08013, doi:10.1029/2008JC005186.

____, W. H. Lipscomb, and A. K. Turner, 2010: Sea-ice models for climate study: Retrospective and new directions. *J. Glaciol.*, **56,** 1162–1172.

____, ____, ____, N. Jeffery, and S. Elliott, 2013: CICE: The Los Alamos sea ice model documentation and software user's manual, Version 5.0. LA-CC-06-012, Los Alamos National Laboratory, 115 pp.

Hurrell, J. W., and Coauthors, 2013: The Community Earth System Model. *Bull. Amer. Meteor. Soc.*, **94,** 1339–1360.

Kaimal, J. C., and J. J. Finnigan, 1994: *Atmospheric Boundary Layer Flows: Their Structure and Measurement*. Oxford University Press, 289 pp.

Lindsay, R. W., 1998: Temporal variability of the energy balance of thick Arctic pack ice. *J. Climate*, **11,** 313–333.

____, 2003: Changes in the modeled ice thickness distribution near the Surface Heat Budget of the Arctic Ocean (SHEBA) drifting ice camp. *J. Geophys. Res.*, **108,** 3194, doi:10.1029/2001JC000805.

Lipscomb, W. H., 2001: Remapping the thickness distribution in sea ice models. *J. Geophys. Res.*, **106,** 13,989–14,000.

Lumley, J. L., and H. A. Panofsky, 1964: *The Structure of Atmospheric Turbulence.* Interscience Publishers, 239 pp.

Mahrt, L., 2010: Computing turbulent fluxes near the surface: Needed improvements. *Agricult. Forest Meteor.*, **150,** 501–509.

Makshtas, A. P., 1991: *The Heat Budget of Arctic Ice in the Winter*. International Glaciological Society, 77 pp.

Maykut, G. A., 1978: Energy exchange over young sea ice in the Central Arctic. *J. Geophys. Res.*, **83,** 3646–3658.

Militzer, J. M., M. C. Michaelis, S. R. Semmer, K. S. Norris, T. W. Horst, S. P. Oncley, A. C. Delany, and F. V. Brock, 1995: Development of the prototype PAM III/Flux-PAM surface meteorological station. Preprints, *Ninth Symp. on Meteorological Observations and Instrumentation*, Charlotte, NC, Amer. Meteor. Soc., 490–494.

Morrison, H., J. A. Curry, M. D. Shupe, and P. Zuidema, 2005: A new double-moment microphysics parameterization for application in cloud and climate models: Part II. Single-column modeling of Arctic clouds. *J. Atmos. Sci.*, **62,** 1678–1693.

Overland, J. E., S. L. McNutt, J. Groves, S. Salo, E. L Andreas, and P. O. G. Persson, 2000: Regional sensible and radiative heat flux estimates for the winter Arctic during the Surface Heat Budget of the Arctic Ocean (SHEBA) experiment. *J. Geophys. Res.*, **105,** 14,093–14,102.

Parkinson, C. L., and W. M. Washington, 1979: A large-scale numerical model of sea ice. *J. Geophys. Res.*, **84,** 311–337.

Paulson, C. A., and W. S. Pegau, 2001: The summertime thermohaline evolution of an Arctic lead. Preprints, *Sixth Conf. on Polar Meteorology and Oceanography*, San Diego, CA, Amer. Meteor. Soc., 271–274.

Perovich, D. K., W. B. Tucker III, and K. A. Ligett, 2002: Aerial observations of the evolution of ice surface conditions during summer. *J. Geophys. Res.*, **107,** 8048, doi:10.1029/2000JC000449.

____, T. C. Grenfell, J. A. Richter-Menge, B. Light, W. B. Tucker III, and H. Eicken, 2003: Thin and thinner: Sea ice mass balance measurements during SHEBA. *J. Geophys. Res.*, **108,** 8050, doi:10.1029/2001JC001079.

Persson, P. O. G., C. W. Fairall, E. L Andreas, P. S. Guest, and D. K. Perovich, 2002: Measurements near the Atmospheric Surface Flux Group tower at SHEBA: Near-surface conditions and surface energy budget. *J. Geophys. Res.*, **107,** 8045, doi:10.1029/2000JC000705.

Sturm, M., J. Holmgren, and D. K. Perovich, 2002: Winter snow cover on sea ice of the Arctic Ocean at the Surface Heat Budget of the Arctic Ocean (SHEBA): Temporal evolution and spatial variability. *J. Geophys. Res.*, **107,** 8047, doi:10.1029/2000JC000400.

Tastula, E.-M., T. Vihma, and E. L Andreas, 2012: Evaluation of Polar WRF from modeling of the atmospheric boundary layer over Antarctic sea ice in autumn and winter. *Mon. Wea. Rev.*, **140,** 3919–3935.

Thorndike, A. S., 1992: A toy model linking atmospheric thermal radiation and sea ice growth. *J. Geophys. Res.*, **97,** 9401–9410.

Treviño, G., and E. L Andreas, 2008: On Reynolds averaging of turbulence time series. *Bound.-Layer Meteor.*, **128,** 303–311.

Uttal, T., and Coauthors, 2002: Surface Heat Budget of the Arctic Ocean. *Bull. Amer. Meteor. Soc.*, **83,** 255–275.

Vickers, D., and L. Mahrt, 1997: Quality control and flux sampling problems for towers and aircraft data. *J. Atmos. Oceanic Technol.*, **14,** 512–526.

Weaver, A. T., and I. Mirouze, 2013: On the diffusion equation and its application to isotropic and anisotropic correlation modelling in variational assimilation. *Quart. J. Roy. Meteor. Soc.*, **139,** 242–260.

Wilks, D. S., 2006: *Statistical Methods in the Atmospheric Sciences*. 2nd ed. Academic Press, 627 pp.